Geosci. Model Dev. Discuss., https://doi.org/10.5194/gmd-2018-286
Manuscript under review for journal Geosci. Model Dev.
Discussion started: 17 December 2018

Geoscientific Model Development Discussions
Open Access
EGU

Max Planck Institute Earth System Model (MPI-ESM1.2) for High-Resolution Model Intercomparison Project (HighResMIP)

Oliver Gutjahr[1], Dian Putrahasan[1], Katja Lohmann[1], Johann H. Jungclaus[1], Jin-Song von Storch[1], Nils Brüggemann[1,2], Helmuth Haak[1], and Achim Stössel[3]

[1]Max Planck Institute for Meteorology, Hamburg, Germany
[2]University of Hamburg, Hamburg, Germany
[3]Department of Oceanography, Texas A&M University, College Station, Texas, USA

Correspondence: O. Gutjahr (oliver.gutjahr@mpimet.mpg.de)

Abstract. As a contribution towards improving the climate mean states of the atmosphere and the ocean in Earth System Models (ESMs), we compare several coupled simulations conducted with the Max Planck Institute for Meteorology Earth System Model (MPI-ESM1.2) following the HighResMIP protocol. Our simulations allow to analyse the separate effects of increasing the horizontal resolution of the ocean (0.4° to 0.1°) and atmosphere (T127 to T255) submodels, and the effects of substituting the Pacanowski and Philander (PP) vertical ocean mixing scheme with the K-Profile Parameterization (KPP).

The results show clearly distinguishable effects from all three factors. The eddy-resolving ocean removes biases in the ocean interior and in the atmosphere. This leads to an important conclusion that ocean eddies have a major impact on the large-scale temperature distribution in the atmosphere, and on temperature and salinity distributions in the ocean. The near-surface wind forcing reduces with a T255 atmosphere and improves ocean mixed layer depths in both hemisphere. The reduced wind forcing further slows the Antarctic Circumpolar Current (ACC) and reduces the transport through Drake Passage to observed values. In the North Atlantic, however, it causes a slow down of the Atlantic Meridional Overturning Circulation (AMOC) due to a slower subpolar gyre, when the PP scheme is used. The KPP scheme causes stronger open-ocean convection that spins up the gyres and leads to a stronger and stable AMOC, when coupled to the T255 atmosphere, maintaining all the positive effects of a higher resolved atmosphere.

1 Introduction

The evolving computational power allows for ever higher resolutions of earth system models (ESM). High resolution ESMs are able to explicitly resolve processes that are subgrid-scale and parameterized in low-resolution models. Optimally, the better resolved processes improve the atmosphere and ocean dynamics and thus reduce biases in the mean state and in the variability of key quantities. In this manuscript we analyse separately the effects of increasing the horizontal atmospheric and oceanic resolution on the mean state. However, besides increasing the resolution of the major model subcomponents, new strategies

Geosci. Model Dev. Discuss., https://doi.org/10.5194/gmd-2018-286
Manuscript under review for journal Geosci. Model Dev.
Discussion started: 17 December 2018

Geoscientific Model Development Discussions
Open Access
EGU

and model developments, such as improved physics, are required for improving ESMs. Therefore, we also analyse the effects of a more sophisticated vertical mixing parameterization in the ocean submodel.

Specifically, this paper describes the adaptation of the Max Planck Institute - Earth System Model (MPI-ESM, Giorgetta et al., 2013) to higher horizontal resolutions and the implementation of improved ocean physics within the PRIMAVERA project (https://www.primavera-h2020.eu/). A key aspect of the project is on improving the simulation of the European climate, which is why we put a focus on the North Atlantic and the Atlantic Meridional Overturning circulation (AMOC). We investigate separately the effects of increasing the horizontal resolution of the atmosphere and the ocean, and of exchanging the vertical mixing parameterization in the ocean and sea ice submodel MPIOM (Jungclaus et al., 2013).

All our simulations follow the High Resolution Model Intercomparison Project (HighResMIP; Haarsma et al., 2016) protocol and provide climate simulations with varying horizontal resolutions that are higher than the standard resolution of the Coupled Model Intercomparison Project - Phase 6 (CMIP6; Eyring et al., 2016).

Our reference model is the MPI-ESM1.2-HR (or HR in the remainder of the manuscript) that was recently described by Müller et al. (2018) and contributes to CMIP6. HR is the higher resolution version of the former MPI-ESM1.2-LR (or LR), with a twice as high (T127, $\sim 100\,\mathrm{km}$) horizontal resolution for the atmospheric submodel ECHAM6.3 (Hertwig et al., 2015; Mauritsen et al., 2018) and a $0.4\,^{\circ}(\sim 40\,\mathrm{km})$ ocean on a eddy-permitting tripolar grid (TP04) (Jungclaus et al., 2013) compared to the LR version (T63, $\sim 200\,\mathrm{km}$ atmosphere and $1.5\,^{\circ}$ ocean grid). How the ocean and atmosphere mean states improve in HR compared to LR were described by Müller et al. (2018). Further reductions of atmospheric biases were shown by Hertwig et al. (2015), who used ECHAM6.3 with a T255 ($\sim 50\,\mathrm{km}$) resolution in atmospheric model intercomparison project (AMIP) type experiments.

Building on these improvements, we further use a coupled MPI-ESM1.2 version with the T255 atmosphere and the TP04 ocean grid (MPI-ESM1.2-XR or simply XR) to investigate the effect of an increased atmospheric resolution on the mean state. This XR version was already used by Putrasahan et al. (2018) and (although under a different acronym) by Milinski et al. (2016). Milinski et al. (2016) demonstrated that the sea surface temperature bias in the upwelling regions along the coast of Africa diminished because of a more detailed representation of the coastal winds with the T255 atmosphere. Although biases were reduced with a T255 version of ECHAM6.3, our XR simulation generally produces too weak surface wind speeds, in particular above the North Atlantic and the subpolar gyre (Putrasahan et al., 2018).

These weaker near-surface winds caused a slowdown of the Atlantic Meridional Overturning Circulation (AMOC) to about $9\,\mathrm{Sv}$ ($\mathrm{Sv} := 10^6\,\mathrm{m}^3\,\mathrm{s}^{-1}$), as documented by Putrasahan et al. (2018). This issue was not only affecting the MPI-ESM1.2, but was also reported by other modelling centres using ECHAM6, although going from T63 to T127 (Sein et al., 2018). Sein et al. (2018) gave a possible explanation for the reduction of mean wind speeds, which they attribute to a higher cyclone activity with the T127 resolution, in particular over the North Atlantic.

The AMOC strength and its stability depend to a large extent on the vertical mixing parameterization (Gent, 2018). To investigate the sensitivity of the AMOC, but also of the mean states, we conducted parallel experiments with HR and XR in which the traditional parameterization of Pacanowski and Philander (1981) (PP scheme) was replaced by the more sophisticated K-Profile Parameterization (KPP) scheme of Large et al. (1994). It turned out that the KPP scheme compensates for the

Geosci. Model Dev. Discuss., https://doi.org/10.5194/gmd-2018-286
Manuscript under review for journal Geosci. Model Dev.
Discussion started: 17 December 2018

Geoscientific Model Development Discussions

underestimated mean winds in the high latitudes and in the tropics in the XR simulation, sustaining a stable AMOC. The reasons for this will be elaborated upon.

Finally, we adopt the $0.1\,^{\circ}(\sim 11\,\mathrm{km})$ tripolar grid (TP6M) of MPIOM that was already used in an eddy-resolving ocean-only simulation forced by NCEP, and in a coupled run with T63 and T255 versions of ECHAM6 – the so-called STORM simulations (von Storch et al., 2012; Stössel et al., 2015, 2018). With this eddy-resolving coupled version (MPI-ESM1.2-ER or ER), we detect noticeable reductions of biases not only in the ocean and near-surface atmosphere, but also in the higher atmosphere. This leads to an important conclusion that ocean eddies have a major impact on the large-scale temperature distribution in the atmosphere, consistent with recent findings (Frenger et al., 2013; Ma et al., 2016; Liu et al., 2018). The parallel simulations allow to separately analyse the effects of atmosphere and ocean model resolution, as well as alternative vertical ocean mixing parameterizations on the mean climate.

We begin by describing the model configuration and spin-up procedure in section 2. In section 3 we present the results of the atmospheric mean state, and in section 4 the results of the ocean mean state. In section 5 we summarize all results.

2 Model, spin-up, and experiments

2.1 Model description

The atmospheric submodel of MPI-ESM version 1.2 is ECHAM6.3 (Mauritsen et al., 2018) and it includes the land-surface scheme JSBACH (Stevens et al., 2013; Reick et al., 2013). The ocean and sea ice submodels are combined in MPIOM (Jungclaus et al., 2013; Notz et al., 2013). ECHAM6.3 and MPIOM are coupled via the Ocean-Atmosphere-Sea-Ice coupler version 3 (OASIS3-mct; Valcke, 2013) with a coupling frequency of 1 h. ECHAM6.3 was used with 95 vertical levels at two different spectral resolutions, truncated at T127 (~103 km) in HR and ER and T255 (~51 km) in XR. We did not change any parameter going from HR to XR, except for a reduction of the time step from 200 s (HR) to 90 s (XR), and the horizontal diffusion damping term. Both use the same eddy-permitting ocean resolution of 0.4°(~44 km) and a tripolar grid (TP04, Jungclaus et al., 2013) with 40 unevenly spaced vertical levels. The first 20 levels are distributed in the top 750 m. A partial grid cell formulation (Adcroft et al., 1997; Wolff et al., 1997) is used for a more accurate representation of the bottom topography. River runoff is calculated by a horizontal discharge model (Hagemann and Gates, 2003).

In the ER configuration, the ocean component has a nominal resolution of $0.1\,^{\circ}$ (~11 km) on a tripolar grid (TP6M) (e.g. von Storch et al., 2012), with higher resolution in the vicinity of the poles. We did not change any parameters compared to the TP04 grid, except that we reduced the time step from 3600 s (TP04) to 300 s (TP6M). Table 1 provides an overview of the simulations that we compared in this study. The HR configuration of our reference simulation is exactly the same as in Müller et al. (2018). The XR configuration was used by Hertwig et al. (2015) (denoted as VHR in their study) for AMIP simulations with ECHAM6 and in Milinski et al. (2016) (denoted as HRatm in their study) for MPI-ESM runs. The ER configuration was already used in stand-alone ocean simulations with 80 vertical levels (von Storch et al., 2012; Stössel et al., 2018), and in fully coupled simulations (e.g. Stössel et al., 2015).

Geosci. Model Dev. Discuss., https://doi.org/10.5194/gmd-2018-286
Manuscript under review for journal Geosci. Model Dev.
Discussion started: 17 December 2018

Geoscientific Model Development Discussions
Open Access
EGU

All simulations (except ER) use the thickness diffusivity κ_{GM} of the Gent et al. (1995) (GM) parameterization to account for the diffusion and tracer advection induced by unresolved mesoscale eddies in the ocean. For the TP04 grid, κ_{GM} is constant and chosen to be proportional to the grid spacing. A value of $\kappa_{GM} = 250\,\mathrm{m^2\,s^{-1}}$ is chosen for a 400 km wide grid cell and it reduces linearly with increasing resolution. That is, for the eddy-permitting TP04 grid κ_{GM} is only about 10 % of this value. The lateral eddy diffusivity is parameterized by an isopycnal formulation (Redi, 1982) and is set to $\kappa_{Redi} = 1000\,\mathrm{m^2\,s^{-1}}$ for a 400 km wide grid cell, again reducing linearly with increasing resolution. In ER, κ_{GM} is set to zero, while κ_{Redi} is unchanged (von Storch et al., 2016).

An innovation over previous versions of HR and XR is that we used two different diapycnal mixing schemes (see section 2.2 for details): the PP scheme as default, and the KPP scheme. The used diapycnal mixing scheme in a simulation is indicated by subscripts: $\mathrm{HR_{pp}}$, $\mathrm{HR_{kpp}}$, $\mathrm{XR_{pp}}$, $\mathrm{XR_{kpp}}$, and $\mathrm{ER_{pp}}$. Note that the model was not retuned when the KPP scheme was used, to account for the pure effect of a changed ocean mixed layer scheme. For all our comparisons, $\mathrm{HR_{pp}}$ is our reference simulation.

We follow the HighResMIP protocol (Haarsma et al., 2016) for initialising and forcing our coupled control simulations. The coupled runs used fixed 1950 forcing that consists of greenhouse gases, including ozone and aerosol loadings of the 1950s climatology ($\sim$ 10 year mean). The HR simulations were initialised from an HR control simulation that was nudged to the averaged state of 1950 to 1954 of the UK MetOffice Hadley Centre EN4 observational data set (version 4.2.0; Good et al. (2013)). The XR runs were initialised from the same ocean state, but from an atmospheric state that has been spun up for 10 years from a dry state. ER was initialised from the HR atmospheric state and directly from EN4 (averaged state from 1950-54) for the ocean. We integrated the HR and XR control simulations for 150 years and the ER simulation for 80 years (see Tab 1). We cut off the first 30 years as spin-up and used the following 50 years from the control runs for the analysis.

2.2 Diapycnal mixing

Previous MPI-ESM versions used a modified version of the Richardson-number dependent formulation of Pacanowski and Philander (1981) (PP scheme). The modification of the original PP formulation consists of a parameterization for wind induced mixing that decays exponentially with depth (Marsland et al., 2003). Convection is parameterized by enhanced eddy diffusivity ($k_v = 0.1\,\mathrm{m^2\,s^{-1}}$). For our simulations here, we corrected a bug associated with the vertical viscosities, which were only about 50 % of the correct solution from the PP scheme. This error was then also corrected in the HR version described by Müller et al. (2018). The background value for the vertical diffusivity is constant and was set to $1.05 \cdot 10^{-5}\,\mathrm{m^2\,s^{-1}}$ and to $5 \cdot 10^{-5}\,\mathrm{m^2\,s^{-1}}$ for the viscosity. The background values represent the breaking of internal waves, which provide the mechanical energy for diapycnal mixing in the interior of the ocean. The PP scheme is the default option in MPI-ESM1.2 and is thus used in our reference simulation ($\mathrm{HR_{pp}}$).

To improve the diapycnal mixing in MPIOM, we implemented the non-local 'K profile parameterization' (KPP, Large et al., 1994). The KPP scheme was implemented by adding the Community Vertical Mixing (CVMix) project library (Griffies et al., 2013) to MPIOM. In the KPP scheme, the turbulent transport do not only depend on local gradients of the properties, but also on the overall state of the boundary layer, that is the surface fluxes and the boundary layer depth (Large et al., 1994). The

Geosci. Model Dev. Discuss., https://doi.org/10.5194/gmd-2018-286
Manuscript under review for journal Geosci. Model Dev.
Discussion started: 17 December 2018

non-local turbulent transport represents how surface properties are redistributed from the surface layer into the boundary layer, for example by buoyant plumes, Langmuir cells, or mesoscale cellular convective elements.

The non-local fluxes are non-zero only for tracers in unstable forcing conditions, i.e. for negative surface buoyancy fluxes. They then directly depend on the net heat and freshwater fluxes crossing the ocean surface multiplied by the local vertical diffusivities, a vertical shape function, and some constants (Griffies et al., 2013). For this non-local fluxes, the same vertical diffusivities are assumed as for the local tracer diffusion. In contrast to the PP scheme, these diffusivities are not limited to a user specified value, but depend on a depth-dependent turbulent vertical velocity scale, on a vertical shape function, and on the mixed layer depth (Griffies et al., 2013).

Below the mixed layer, we use the PP scheme with the same constant background diffusivity and viscosity. The diffusivities are not matched at the base of the mixed layer. Under sea ice, we reduce the wind induced mixing in the PP and in the KPP scheme, so that the surface friction velocity u_* decreases with increasing sea ice concentration. For simplicity, we neglect that the momentum flux from the atmosphere into the ocean could be even stronger when sea ice is present, because of additional momentum flux at the interface of sea ice and the underlying sea water.

3 Evaluation of the atmospheric mean state

For the evaluation, the MPI-ESM1.2 simulations were averaged over the first 50 model years after the spin-up. We used the ERA-Interim reanalysis data (Dee et al., 2011) averaged from 1979–2005 as reference for the atmospheric mean state, as HR was tuned to this period (Mauritsen et al., 2012).

3.1 Surface quantities

3.1.1 10 m wind speed

The simulated 10 m wind speed agrees well with ERA-Interim for large parts of the world's oceans and over the continents (Fig. 1). Consistently too low wind speeds, however, evolve over the northern parts of America and Europe, over South America, and over Greenland and Antarctica. Too strong winds are simulated by all models over the subtropical oceans north and south of the equator. Models with the T127 atmosphere further simulate too strong winds speeds over the Weddell Sea (Fig. 1b,c,f).

Although the KPP scheme has only a minor effect on the 10 m wind speed, in some areas KPP reduces the biases. For example, HR_{kpp} (Fig. 1c) reduces the positive bias in the subtropical Atlantic and North Pacific. At the equatorial Pacific, KPP reverses the negative bias to a positive wind speed bias. Further, the negative bias in the Denmark and Fram Strait is reduced because of lower sea ice concentration in this area (see section 4.4).

Increasing the horizontal resolution from T127 to T255 in XR_{pp} (Fig. 1d) introduces a negative wind speed bias over the Antarctic Circumpolar Current (ACC) because of a reduced meridional pressure gradient over the subpolar gyre in the North

Geosci. Model Dev. Discuss., https://doi.org/10.5194/gmd-2018-286
Manuscript under review for journal Geosci. Model Dev.
Discussion started: 17 December 2018

Atlantic, and over the Nordic Seas. This reduced wind forcing over the subpolar gyre causes a slowdown of the AMOC in XR_{pp}, as described in detail by Putrasahan et al. (2018) and briefly outlined in section 4.

By using the KPP scheme in the XR model (XR_{kpp}; Fig. 1e), the wind speed reduces in the same areas as mentioned above, but not as strong as in XR_{pp}. This indicates that KPP can sustain a sufficient mixing to prevent a decline of the AMOC albeit a weaker wind forcing (as discussed later). However, the wind speed is still lower over the Nordic Seas and in the Pacific sector of the ACC. This reduced wind forcing of the ACC decreases the transport through the Drake passage as discussed later. Other regions are much less unaffected.

Increasing the horizontal resolution of MPIOM from 0.4° to 0.1° (ER_{pp}; Fig. 1f) reduces the positive bias over the Indian Ocean, over the Greenland Sea, and over the subtropical Atlantic. Despite these improvements, an eddy-resolving ocean does have only a minor effect on the near-surface wind speed, when coupled to a rather coarse T127 atmospheric resolution.

3.1.2 2 m temperature

In contrast to the near-surface wind speed, the 2 m temperature distribution (Fig. 2) is stronger affected by changing the horizontal resolution of the submodels or by replacing the vertical ocean mixing parameterization. It closely resembles the bias of the sea surface temperature (section 4.1.1). Again, all models (except XR_{pp}) agree well with ERA-Interim over the continents and over large parts of the world's oceans, in particular over the tropical and subtropical oceans and in the Arctic Ocean.

An area with larger discrepancies across all models is the North Atlantic. Here, all simulations show a cold bias, which is a common error in state-of-the-art ESMs (Dengg et al., 1996), which is caused by a too zonal North Atlantic Current (NAC) (see section 4.1.1). Another area of cold near-surface temperature biases is Antarctica and its peninsula. All models (except XR_{pp}) simulate a consistent warm bias over the Canadian Archipelago, central Africa and central Asia. Although reducing in its magnitudes, all these biases remain in the higher resolution models or when KPP is used.

Our models with the T127 atmosphere (Fig. 2b,c,f) simulate further a warm bias over the Weddell Sea, which is caused by too frequent open polynyas (see section 4.5). This warm bias vanishes, partly changing its sign in the western Weddell Sea, when increasing the atmospheric resolution to T255 in the XR models (Fig. 2d,e). This is because the frequency of open-ocean polynyas reduces (see section 4.5), so that the Weddell Sea is more often covered with thicker ice (not shown), causing colder near-surface temperatures. However, a severe cold bias develops over the North Atlantic and the Nordic Seas in XR_{pp}, as mentioned before. As a consequence, the temperatures over Europe decrease as well.

Using the KPP scheme in HR (Fig. 2c) results in warmer 2 m temperatures in the northern hemisphere, so that cold biases reduce, but warm biases become stronger. The reason is a stronger northward heat transport into the North Atlantic (see section 4) and thus a stronger heat release to the atmosphere. In XR_{kpp} (Fig. 2e), the warming caused by the KPP scheme and the cooling caused by the T255 atmosphere compensate, so that the bias pattern in the northern hemisphere is comparable to that of HR_{pp}. The cold bias along the ACC, however, is not affected by KPP and similar to XR_{pp}.

Geosci. Model Dev. Discuss., https://doi.org/10.5194/gmd-2018-286
Manuscript under review for journal Geosci. Model Dev.
Discussion started: 17 December 2018

Geoscientific Model Development Discussions

Although ER_{pp} (Fig. 2f) produces a similar bias pattern as HR_{kpp}, because of the same T127 atmosphere, it clearly reduces the cold bias over the ACC in the Southern Ocean due to partly resolved eddies. The warm bias in the Weddell Sea, however, is slightly enhanced in the Atlantic sector of the Southern Ocean.

3.2 Vertical structure of zonal wind speed and temperature

3.2.1 Zonal wind speed

Fig. 3 shows the ERA-Interim climatology of the time-mean zonal-mean wind speed (u-velocity) and the model biases. Overall, the vertical structure of the zonal wind speed is well represented in MPI-ESM1.2. A consistent bias of all simulations are too strong subtropical jets (centred at $\sim 200\,\mathrm{hPa}$). These enhanced jets contribute further to higher zonal wind speeds extending into the upper troposphere at 40 to $45\,^{\circ}\mathrm{S}$ and 40 to $45\,^{\circ}\mathrm{N}$, as found by Müller et al. (2018). Another positive bias is simulated in the middle of the tropical troposphere (at $\sim 400\,\mathrm{hPa}$).

All models simulate a consistent negative bias over the Southern Ocean at $\sim 60\,^{\circ}\mathrm{S}$ that extends through the whole troposphere. Although KPP reduces the bias over the Southern Ocean in HR_{kpp} (Fig. 3c) and increases slightly the biases in the upper troposphere, the overall pattern is very similar to HR_{pp} (Fig. 3b). The T255 atmosphere in the XR models amplifies all biases (Fig. 3d-e). That is, the subtropical jets become stronger and shift equatorwards and the zonal wind speed over the Southern Ocean reduces further.

Important for the ocean is the extension of the negative bias over the Southern Ocean down to the surface (except in ER_{pp}), which directly reduces the wind forcing of the ocean. Note that the near-surface negative bias for the North Atlantic cannot be seen here, as discussed above, because it cancels in the zonal mean. On the other hand, the eddy-resolving ocean does not modify the mean zonal wind speed (Fig. 3f).

3.2.2 Zonal temperature

The cross sections of the time-mean zonal-mean temperature (Fig. 4) show cold biases in the upper troposphere (at $\sim 250\,\mathrm{hPa}$) in both hemispheres. In the simulations with PP, the cold bias extends to the surface in both hemispheres (Fig. 4b,d), whereas with KPP only in the southern hemisphere (Fig. 4c,e).

In XR_{pp} the cold bias becomes larger in the lower troposphere, because of the slowing down of the AMOC and the freezing of the Labrador and Nordic Seas (see section 4 below). In contrast, the AMOC remains stable in XR_{kpp} (Fig. 4e), so that no severe cold bias evolves in the lower troposphere of the northern hemisphere. However, the KPP scheme does not affect the cold bias in the southern hemisphere, as already found for the 2 m temperature. A clear improvement can be seen in ER_{pp} (Fig. 4f), which removes both biases in the lower and middle troposphere in both hemispheres. We conclude that eddies play a major role for the large-scale temperature distribution in the atmosphere.

Geosci. Model Dev. Discuss., https://doi.org/10.5194/gmd-2018-286
Manuscript under review for journal Geosci. Model Dev.
Discussion started: 17 December 2018

4 Evaluation of the ocean mean state

4.1 Ocean surface temperature and salinity

4.1.1 Sea surface temperature

The sea surface temperature bias to the UK MetOffice EN4 data (version 4.2.0; Good et al. (2013), averaged from 1945–1955) is shown in Fig. 5. We used this period for EN4 since our HR simulations were initialised from a simulation that was nudged to the averaged EN4 state of 1950–54, and we further allow for some variance. The results differ only marginally if another period is chosen (not shown). In general, biases occur in prominent areas and are affected by both changing the model resolution and the diapycnal mixing scheme.

All simulations (except XR_{pp}) simulate realistic sea surface temperatures in comparison to EN4 (Fig. 5). Colder sea surface temperatures of about 1 to $2\,^{\circ}\mathrm{C}$ than in EN4 are simulated in the northern hemisphere in HR_{pp} (Fig. 5b). The strongest cold bias of up to $-7\,^{\circ}\mathrm{C}$ occurs in the North Atlantic between $40\,^{\circ}\mathrm{N}$ to $50\,^{\circ}\mathrm{N}$, centred at about $30\,^{\circ}\mathrm{W}$. A similar magnitude was described by Müller et al. (2018) for MPI-ESM1.2-HR. The explanation for this cold bias is a too zonal NAC (Dengg et al., 1996), causing a too far southward intrusion of fresh and cold Labrador Sea water (Müller et al., 2018). Too cold sea surface temperatures are further simulated along the ACC (bias of $\sim 2\,^{\circ}\mathrm{C}$). Coastal upwelling areas west of Africa and South America are about 1 to $2\,^{\circ}\mathrm{C}$ too warm in all simulations with the T127 atmosphere (Fig. 5b,c,f), as found by Milinski et al. (2016)

Increasing the atmospheric resolution from T127 to T255, while using the PP scheme (XR_{pp}), causes a severe cold bias in the whole northern hemisphere (Fig. 5d), strongest in the North Atlantic ($-9\,^{\circ}\mathrm{C}$). This cooling was already described by Putrasahan et al. (2018) and is caused by a slowed AMOC due to too weak wind stress over the subpolar gyre and too weak northward heat and salt transports (see also Tab. 4 and section 4.6). Although the reduced wind forcing over the Southern Ocean (Fig. 1) might also contribute to a weakening of the AMOC (Toggweiler and Samuels, 1995) in XR_{pp}, Putrasahan et al. (2018) found no effect of this negative wind bias on the AMOC slow down, and argue that the timescale of the slowing AMOC is much faster than any feedback from the Southern Ocean to the North Atlantic.

On the other hand, the biases in the coastal upwelling areas diminished to some extent, because of the better resolved coastal wind systems. This warm bias reduction in the upwelling areas is consistent with other studies (Putrasahan et al., 2013; Small et al., 2015; Milinski et al., 2016). Furthermore, the Pacific cold-tongue almost disappears, but now the tropical Pacific becomes too warm south of the equator.

The KPP scheme reduces the cold bias in the North Atlantic in HR_{kpp} (Fig. 5c), but enhances a warm bias in the Labrador Sea and in the Nordic Seas because of an increased heat transport into the North Atlantic and its ambient seas. Moreover, a warm bias evolves in the tropical Pacific north and south of the equator. However, the KPP scheme simulates a stable AMOC in XR_{kpp} (Fig. 5e), because of a stronger subpolar gyre (see Tab. 2). The enhanced deep convection and North Atlantic Deep Water (NADW) formation in the Labrador Sea (section 4.5) sustains a strong enough upper cell of the AMOC (section 4.6) and thus a sufficient northward transport of heat and salt (see also Tab. 4). This surplus in heat and salt transports, compared to XR_{pp}, prevents the Labrador Sea from freezing over. This finding is an important result and provides a solution to the declining

Geosci. Model Dev. Discuss., https://doi.org/10.5194/gmd-2018-286
Manuscript under review for journal Geosci. Model Dev.
Discussion started: 17 December 2018

AMOC strength for MPI-ESM1.2-XR. In addition, enhanced upwelling in the Southern Ocean further strengthens the northern cell of the AMOC (Marshall et al., 2017), although it is not the main reason in our model.

ER_{pp} clearly reduces the cold bias along the ACC (Fig. 5f), because of resolving eddies that flatten and shift the outcropping isopycnals southwards. It further reduces the cold bias in the North Atlantic, in the North Pacific, and in the Mediterranean Sea. The biases in the upwelling regions, however, remain because of the coarse T127 atmosphere.

4.1.2 Sea surface salinity

As with sea surface temperature, the sea surface salinity is well simulated with MPI-ESM1.2 for most parts of the ocean with respect to EN4 (Fig. 6). However, in some areas we find larger discrepancies. In the North Atlantic, the surface waters are too fresh where we already found a cold bias. This freshwater bias is again caused by the too zonal NAC and the entrainment of fresher water masses from the Labrador Current. Although all models produce this bias, its magnitude differs with respect to HR_{pp} (Fig. 6a) by either increasing the model resolution or by replacing the vertical mixing scheme in the ocean.

Both the KPP scheme (Fig. 6c) and the eddy-resolving ocean reduce the freshwater bias in the North Atlantic, because of a stronger northward salt transport by the NAC and because more saline waters are exported from the Labrador Sea along the Deep Western Boundary Current.

In case of ER_{pp}, the Gulf Stream separation is better represented, which further reduces the bias in the North Atlantic (Fig. 6f). The resolved eddies further remove the freshwater bias along the ACC. The water masses in the Mediterranean Sea become more saline, which removes the freshwater bias that the HR and XR models produce.

Increasing the atmospheric resolution from T127 to T255 enhances the freshwater bias in XR_{pp} (Fig. 6d) because of the above described AMOC slow down, with the consequence that less salt is transported by the Gulf Stream and the NAC into the North Atlantic. In XR_{kpp} (Fig. 6e), both effects work in opposite directions and almost balance each other, so that the bias is similar to that in HR_{pp}

Another bias present in all simulations is a too saline Arctic Ocean, originating from the Siberian coast that extends across the Transpolar Drift, but also into the Canadian basin. These too saline waters indicate too little freshwater input from the Siberian rivers, in particularly from the Lena river (Laptev Sea). Another effect that enhances this error could be too little barotropic tidal mixing along the Arctic shelves and thus too less horizontal spreading of the river waters (Wang et al., 2014).

Finally, a strong freshwater bias is simulated in the western Pacific. The KPP scheme seems not to modify this bias, but the surface waters become severely fresher in both XR simulations. Since there is no obvious difference in precipitation or evaporation (not shown), we suspect that the supply of salty waters from the east reduces in XR. Although still too fresh, ER_{pp} reduces this bias.

4.2 Ocean interior

Figure 7 shows the time-mean zonal-mean temperature bias of the MPI-ESM1.2 simulations to EN4 for the Atlantic and the Arctic Ocean. The bias of the HR and XR simulations are very similar and show a maximum warm bias at roughly $40\,^{\circ}\mathrm{S}$, continuing to $30\,^{\circ}\mathrm{N}$ at depths of the AAIW (about 800 to 1000 m). These biases are thought to be caused by erroneous interior

Geosci. Model Dev. Discuss., https://doi.org/10.5194/gmd-2018-286
Manuscript under review for journal Geosci. Model Dev.
Discussion started: 17 December 2018

circulation, tracer advection and mixing due to unrepresented eddy-induced tracer transports (Griffies et al., 2009; Jungclaus et al., 2013).

The warm bias at $40\,^{\circ}\mathrm{S}$ is related to too much advection of warm and salty waters from the Indian Ocean (Jungclaus et al., 2013), because the resolution is still too low to represent the Agulhas Current system, with its retroflection and intermittent eddy shedding that transfers heat and salt into the Atlantic. In the HR/XR configurations with the TP04 grid, a constant Agulhas leakage transports warm and salty water, instead. Neither the KPP scheme (Fig. 7c) nor the T255 atmosphere (Fig. 7d,e) reduces this warm bias. It reduces only with the eddy-resolving ocean grid (TP6M) in $\mathrm{ER_{pp}}$ (Fig. 7f), as reported by von Storch et al. (2016) for ocean-only simulations. There are two reasons for this warm bias reduction in $\mathrm{ER_{pp}}$: (1) the Agulhas Return Current and the Agulhas leakage are now better resolved, producing a more realistic circulation and water mass transfer from the Indian Ocean into the South Atlantic, as seen in other similar studies (McClean et al., 2011; Putrasahan et al., 2016; Cheng et al., 2018); and (2) the eddy-induced cooling and freshening of the intermediate ocean (von Storch et al., 2016) further reduces the warm bias.

The warm bias in Fig. 7a-e stretches northward at the depth of the Antarctic Intermediate Water (AAIW) and shows another maximum at $30\,^{\circ}\mathrm{N}$ that is related to the spreading of Mediterranean waters. The HR and XR models use the same TP04 ocean grid and simulate both the observed net volume transport through the Strait of Gibraltar (net inflow of about $0.04\,\mathrm{Sv}$; see Tab. 3). In the TP04 grid, the strait is about 54 km wide with a sill depth of about 230 m. The outflowing Mediterranean water is too warm and too saline in all HR and XR simulations compared to EN4, which explains the warm and saline bias (Fig. 8a-e). In $\mathrm{HR_{kpp}}$, the Mediterranean water is slightly more saline than in $\mathrm{HR_{pp}}$, so that the water spreading northward along the European continental shelf becomes also more saline and contributes to saltier Northeastern Atlantic Deep Water. This enhanced flow of saline water into the subpolar gyre explains the reduced salinity bias at 40 to $50\,^{\circ}\mathrm{N}$ at a depth of 1000-1500 m (Fig. 8c). The main spreading pathway in all HR and XR models, however, is to the southwest into the open Atlantic.

As with the warm biases, the salinity biases reduce in $\mathrm{ER_{pp}}$. A fresher water mass at intermediate depth reflects a much more realistic representation of the AAIW (Fig. A3) and of the outflow of Mediterranean water. The latter is less saline and about 2 to $3\,^{\circ}\mathrm{C}$ colder (not shown), reducing the warm and saline bias at $30\,^{\circ}\mathrm{N}$ (Fig. 7f and Fig. 8f). The reason for this major improvement is the better resolved bathymetry of the Strait of Gibraltar, which is about 24 km wide in the TP6M grid. Although the salinity maximum of the overflow water is about 100 m shallower than in EN4 (not shown), $\mathrm{ER_{pp}}$ produces more realistic properties of upper and intermediate depth water masses.

The too zonal NAC causes a cold and fresh bias between 40 to $50\,^{\circ}\mathrm{N}$ in the upper ocean (above 1000 m depth) in all simulations (Fig. 7 and Fig. 8). Although the Gulf Stream separates earlier from the American coast in $\mathrm{ER_{pp}}$ (not shown), its flow path is still too zonal, such that the cold bias in the North Atlantic improves only marginally. The too warm and saline subpolar gyre causes a warm and saline bias in the deep convection areas, centred around $60\,^{\circ}\mathrm{N}$. The bias increases in $\mathrm{HR_{kpp}}$ because of the increased transport of heat and salt from the Subtropical Gyre into the subpolar gyre. The bias reduces in the XR models because of the weaker subpolar gyre and reduced salt transport by the gyre. However, from Fig. 8d, we see that the reduced salinity is the main factor causing the reduced convection in $\mathrm{XR_{pp}}$, as described by Putrasahan et al. (2018). Another

Geosci. Model Dev. Discuss., https://doi.org/10.5194/gmd-2018-286
Manuscript under review for journal Geosci. Model Dev.
Discussion started: 17 December 2018

Geoscientific Model Development Discussions

contribution is too warm and saline overflow waters from the Nordic Seas, an issue that was also present in coarser MPI-ESM versions (Jungclaus et al., 2013). The bias is mostly unaffected in ER_{pp}.

The Atlantic water entering the Arctic Ocean ($0\,^{\circ}C$ potential temperature bounds in Fig. 7a) is too warm and its layer is too thick in all HR and XR simulations (Fig. 7b-e), causing a warm bias within the Atlantic layer between 200 m to 1000 m. This is a common error in ocean general circulation models (Ilicak et al., 2016), which is thought to be caused by spurious numerical mixing of the advection operator (Holloway et al., 2007). Zhang and Steele (2007) further found a direct impact of the vertical mixing strength onto the circulation of the Atlantic Water into the Arctic Ocean. Reducing the vertical mixing in the European Basin reduces the diffusion of the Atlantic Water and results in a thinner layer. By comparing the vertical mixing across all our simulations (Fig. A1) we see that ER_{pp} simulates less vertical mixing in the Arctic Ocean at the depth of the Atlantic Water layer (as well as in the deeper layers of the Arctic Ocean and Atlantic).

Further, less vertical mixing in the Fram Strait can reduce the inflow of Atlantic Water into the Arctic Ocean (Zhang and Steele, 2007) and thus reduce the warm bias as ER_{pp} does. In fact, Zhang and Steele (2007) recommend to reduce the background diffusivity to $1 \cdot 10^{-6}\,m^2\,s^{-1}$ and viscosity to $1 \cdot 10^{-5}\,m^2\,s^{-1}$. The background value for diffusivity is thus an order of magnitude lower than in our configuration. However, our results show that an eddy-resolving resolution the in the Arctic Ocean removes the warm and saline bias in the Atlantic Water layer, without changing any background values for vertical mixing. That a very high-resolution is necessary for the Arctic Ocean was recently shown by Wang et al. (2018) as well, who used a background diffusivity of $1 \cdot 10^{-5}\,m^2\,s^{-1}$, which is close to what we chose. In contrast, for example Sein et al. (2018) chose to reduce the background value by one order of magnitude.

4.3 Ocean circulation

To evaluate the large-scale ocean circulation, we compared barotropic stream functions of selected regions, transports through straits, and the AMOC. Overall we find three effects: (1) increasing the atmospheric resolution to T255 reduces the gyre strengths, (2) the KPP scheme enhances the strength of all gyres, and (3) the effect of an eddy-resolving ocean is bi-directional.

The simulated subpolar gyre strengths range from 31.0 to $40.6\,Sv$ and are all within the observational range of 26.0 to $40.0\,Sv$ (Tab. 2). HR_{kpp} simulates a slightly stronger subpolar gyre than the reference simulation HR_{pp}. Both XR_{pp} and XR_{kpp} show a clear drop of the gyre strength with a T255 atmosphere, as described by Putrasahan et al. (2018). In contrast, increasing the ocean resolution to eddy-resolving (ER_{pp}) does not affect the subpolar gyre strength noticeably.

The volume transport of the Subtropical Gyre in the North Atlantic, however, reacts more sensitive to the chosen vertical ocean mixing scheme and the eddy-resolving resolution. Compared to the reference of $48.2\,Sv$ (HR_{pp}), the gyre strength only slightly reduces to $44.0\,Sv$ with a higher atmospheric resolution (XR_{pp}). By using the KPP scheme, however, the gyre strength increases to $64.9\,Sv$ (HR_{kpp}) and remains similarly high with a T255 atmosphere (XR_{kpp}). ER_{pp} produces a gyre strength as strong as with the KPP scheme. However, compared to observations (46.0 to $61.0\,Sv$), ER_{pp} and the simulations with KPP simulate slightly stronger transport. In the case of HR_{kpp} and XR_{kpp} this might explain the positive salinity bias in the North Atlantic. Similar findings results for the Subtropical Gyre in the Pacific, except that ER_{pp} reduces the gyre strength.

Geosci. Model Dev. Discuss., https://doi.org/10.5194/gmd-2018-286
Manuscript under review for journal Geosci. Model Dev.
Discussion started: 17 December 2018

Geoscientific Model Development Discussions
Open Access
EGU

Tab. 3 summarizes the transports through important passages. The net volume transport through the Bering Strait is of the same magnitude (0.6 to 0.7 Sv) for HR_{pp}, HR_{kpp} and XR_{kpp}, which is on the lower side of the observations (0.7 to 1.1 Sv). The transport is even lower (0.5 Sv) in XR_{pp}, which indicates a low exchange of the Arctic Ocean and the Pacific. Increasing the ocean resolution leads instead to a higher transport of 0.9 Sv in ER_{pp}.

The net transport through Fram Strait, however, is too low in all simulations and reduces further with either an eddy-resolving grid or the KPP scheme. A possible explanation for this reduced transport with KPP is given by Zhang and Steele (2007). They found that strong vertical mixing, as with the KPP scheme in our HR and XR simulations, deepens the Atlantic Water layer, but simultaneously weakens the inflow strength of Atlantic Water and the outflow strength of Arctic Water. However, the transport by ER_{pp} is even lower. The reason for this has to be further investigated.

The overflows through Denmark Strait and across the Iceland-Scotland ridge are important deep water connections for the Arctic and the Atlantic. Although all simulations produce realistic overflow values with respect to observations, we found systematic effects of either increasing the model resolution or using KPP. Both, increased model resolution and the KPP scheme increase the strength of overflows. In particular the eddy-resolving ocean (ER_{pp}) produces more overflow waters. In the case of HR_{kpp}, this higher transport is caused by enhanced deep convection in the Nordic Seas, particularly in the Greenland Sea (Fig. 10).

In all HR and XR simulations, the volume transport of the Florida Current is only about half the observed value of roughly 32 Sv (Tab. 3). Although the transport increases with the KPP scheme, only ER_{pp} strengthens the transport considerably to 25 Sv. This indicates that the eddy-resolving ocean has a clear impact on this current. We found similar results for the Indonesian throughflow, which is important for climate because it connects the Pacific with the Indian Ocean and closes the upper warm branch of the MOC. Again KPP enhances the transports slightly, but only ER_{pp} simulates a transport strength that is similar to observed values.

The Mozambique channel is an example where both a T255 atmosphere and KPP show a reduction in the transports. In ER_{pp}, however, the transport is about twice as high as in the other simulations and more realistic with respect to recent observations of 16.7 ± 8.9 Sv (Ridderinkhof et al., 2010). The ability to resolve eddies, particularly the Mozambique eddies along with a better resolved southward advection throughout the Mozambique Channel likey contributes to the more realistic transport of about 14 Sv in ER_{pp} (Putrasahan et al., 2016; Ridderinkhof et al., 2010).

The observed baroclinic transport through the Drake Passage was usually stated as roughly 140 Sv. However, recently a new estimate reveals a much higher transport volume of about 173.3 ± 10.7 Sv, if the barotropic transport is added (Donohue et al., 2016). With regard to this estimation, the models are within or close to the observed estimation. However, compared to the reference simulation HR_{pp} (161.1 Sv) the transport reduces to about 150.0 Sv in XR_{pp}, and from 191.9 Sv in HR_{kpp} to 170.3 Sv in XR_{kpp}. In ER_{pp} the transport is lower than in all other models with 140.9 Sv. These results confirm that a higher atmospheric or ocean resolution reduces the transport in the Drake Passage, as described by Stössel et al. (2015), while the KPP scheme enhances the transport, probably because of enhanced deep convection in the Weddell Sea that steepens the isopycnals across the ACC and thus increases the geostrophic flow (Stössel et al., 2015; Naughten et al., 2018) (see section 4.5.2).

Geosci. Model Dev. Discuss., https://doi.org/10.5194/gmd-2018-286
Manuscript under review for journal Geosci. Model Dev.
Discussion started: 17 December 2018

4.4 Sea ice

4.4.1 Arctic Ocean

The sea ice thickness distribution agrees well with the PIOMAS reanalysis (Zhang and Rothrock, 2003; Schweiger et al., 2011) (not shown) and is comparable to the MPI-ESM1.2-HR simulation described by Müller et al. (2018). The maximum ice thickness (multi-year ice) in March is generally found along the north coast of Greenland and the Canadian Archipelago (Fig. 9), and reaches about $3\,\mathrm{m}$ in $\mathrm{HR_{pp}}$. The ice cover in $\mathrm{HR_{pp}}$ reaches far south to Iceland in the Denmark Strait, as described by Müller et al. (2018), but remains close to Greenland's coast in $\mathrm{HR_{kpp}}$ (Fig. 9b). The enhanced northward heat transport into the Nordic Seas in $\mathrm{HR_{kpp}}$ results in warmer sea surface temperatures, leading to a northward shift of the winter ice edge. Further, a stronger recirculating branch of the West Spitsbergen Current in the Fram Strait (not shown) in $\mathrm{HR_{kpp}}$ pushes the East Greenland Current westwards to the east coast of Greenland, which narrows and becomes faster, so that sea ice is constrained to a narrower band along the coast. The sea ice thickness reduces also in the Eurasian Basin by about $0.25\,\mathrm{m}$ to $0.5\,\mathrm{m}$ in $\mathrm{HR_{kpp}}$, while it becomes thicker in the Canadian Basin by the same amount.

$\mathrm{XR_{pp}}$ (Fig. 9c) simulates much more sea ice reaching the north coasts of Iceland because of the above described fresher and colder North Atlantic and the resulting freeze-over of the Labrador Sea. Instead, $\mathrm{XR_{kpp}}$ (Fig. 9d) simulates thicker sea ice in the Denmark and Fram Strait because of colder sea surface temperatures. In contrast to $\mathrm{HR_{kpp}}$, the recirculating branch of the West Spitsbergen Current does not become not stronger in $\mathrm{XR_{kpp}}$ (and $\mathrm{XR_{pp}}$). In addition, the near-surface circulation in the Arctic Ocean changes with a T255 atmosphere from a more anticyclonic circulation in the Makarov and Canadian Basin in HR, to a more cyclonic circulation in XR (not shown). A cyclonic circulation enhances the export of cold Arctic Water via the East Greenland Current, causing colder sea surface temperatures in the Nordic Seas. Both XR models and $\mathrm{ER_{pp}}$ simulate thinner winter ice in the Canada Basin as well. For both XR it can be explained by an enhanced ice export due to the more cyclonic circulation mentioned above. For $\mathrm{ER_{pp}}$, however, it needs to be investigated.

The extent of the Arctic summer ice cover in September is less in the XR than in the HR models (not shown), in particular over the Siberian shelves, which is probably caused by the better resolved T255 atmosphere. KPP again simulates thinner ice in the Canada basin (about $-0.5\,\mathrm{m}$).

4.4.2 Southern Ocean

The austral winter (September) sea ice thickness distribution in the Southern Ocean of $\mathrm{HR_{pp}}$ (not shown) is similar to the MPI-ESM1.2-HR described by Müller et al. (2018). The ER and both HR simulations produce an overabundance of open-ocean polynyas in the Weddell Sea (see section 4.5.2). $\mathrm{HR_{kpp}}$ simulates less and thinner ice in the Weddell Sea than $\mathrm{HR_{pp}}$, but otherwise the spatial distribution of sea ice in the Southern Ocean is very similar.

Both XR simulations, but more so $\mathrm{XR_{pp}}$, produce thicker sea ice than the other simulations, in particular in the Weddell Sea and close to Antarctica's coasts. The thicker ice in the Weddell Sea emerges in concert with a reduced number of polynyas, so that the warm bias seen in Fig. 2 vanishes. This less frequent occurrence of Weddell Sea polynyas is probably related to a reduced meridional pressure gradient across the Weddell Sea and the ACC (not shown), which in turn reduces the near-surface

Geosci. Model Dev. Discuss., https://doi.org/10.5194/gmd-2018-286
Manuscript under review for journal Geosci. Model Dev.
Discussion started: 17 December 2018

wind speed forcing (as seen in Fig. 1) for the polynya. However, a more detailed investigation is required to explain circulation differences between the T127 and the T255 over the Weddell Sea. In austral summer, the sea ice extends further into the Weddell Sea in both XR simulations (not shown).

4.5 Mixed layer depth and diapycnal mixing

4.5.1 Northern hemisphere

The average surface mixed layer depths in March for the northern hemisphere are shown in Fig. 10. We diagnosed the mixed layer depth as the depth where the density deviates from the surface density by $\sigma_t = 0.01\,\mathrm{kg\,m^{-3}}$. This diagnostic was computed from monthly means.

In the reference simulation $\mathrm{HR_{pp}}$ (Fig. 10a), average depths of up to $1500\,\mathrm{m}$ are simulated in the Labrador Sea, and up to $600\,\mathrm{m}$ south of Cape Farewell, in the Irminger Sea, and in the Nordic Seas. As discussed before, in $\mathrm{XR_{pp}}$ (Fig. 10c) the deep convection ceases in the Labrador Sea and in the Nordic Seas, leading to a slowing down of the AMOC (Tab. 4). The KPP scheme in $\mathrm{HR_{kpp}}$ (Fig. 10b) causes much deeper mixed layers in the Labrador Sea and mixed layers depths of about $1000\,\mathrm{m}$ in the Greenland Sea. In particular the convection area in the Labrador and Irminger Sea south of Greenland (north of $50\,^\circ\mathrm{N}$) becomes deeper compared to all other models. These deeper mixed layers with the KPP scheme result on one hand from the convection parameterization (i.e. the non-local fluxes) and on the other hand from a stronger and more cyclonic subpolar gyre that domes the isopycnals in the gyre centres (not shown), which preconditions the water column for convection.

As mentioned in section 2.2, the non-local fluxes in the KPP scheme use the same vertical diffusivities as for the local gradient transports. These diffusivities are not limited to a user-defined maximum value during convective forcing conditions, so that much larger diffusivities can act to redistribute temperature and salinity, causing the water column to overturn faster and to produce deeper mixed layers in the KPP than in the PP scheme.

On the other hand, $\mathrm{XR_{kpp}}$ (Fig. 10d) simulates shallower mixed layers compared with $\mathrm{HR_{kpp}}$. These shallower mixed layers result from the reduced wind stress of the T255 atmosphere by means of two processes: (1) lower wind stress spins down the subpolar gyre, so that the slower cyclonic circulation reduces the isopycnal doming and the horizontal salt advection to the gyre centres, leading to a more stratified surface layer; and (2) lower near-surface wind speeds reduce the turbulent air-sea fluxes via the bulk formula and the surface friction velocity (u_*). Lesser heat fluxes in turn reduce directly the non-local fluxes of the KPP scheme in convection areas, and lower u_* reduces the turbulent vertical velocity scales, which results in lower vertical diffusivities and viscosities.

Based on these results, increasing the atmospheric resolution reduces the mixed layer depths over the North Atlantic and the Nordic Seas, whereas KPP deepens them. By combining both, the T255 atmosphere and the KPP scheme, the above effects compensate ($\mathrm{XR_{kpp}}$; Fig. 10d). In contrast to $\mathrm{XR_{pp}}$, where the convection ceases in the Labrador and GIN Seas, the combination of T255 and KPP ($\mathrm{XR_{kpp}}$) produces more realistic mixed layers depths even with reduced wind forcing.

Overall, the KPP scheme influences the large-scale circulation, which in turn provides favourable conditions for deep convection in the Labrador Sea, Irminger Sea, and Nordic Seas. For this reason, $\mathrm{HR_{kpp}}$ and $\mathrm{XR_{kpp}}$ simulate enhanced deep convection

Geosci. Model Dev. Discuss., https://doi.org/10.5194/gmd-2018-286
Manuscript under review for journal Geosci. Model Dev.
Discussion started: 17 December 2018

compared with HR_{pp} and thus mixed layers deeper of about 500 to 600 m in the Irminger Gyre, which is consistent with observations (e.g. Pickart et al., 2003; Våge et al., 2008, 2011). The deeper mixed layers in the Irminger Sea in XR_{kpp} are probably linked to better resolved Greenland tip jets, although a T255 is still too coarse to resolve them sufficiently (Gutjahr and Heinemann, 2018).

Except for XR_{pp}, the maximum mixed layer depths are nevertheless too deep. A possible explanation is the neglect of tidal mixing in MPI-ESM1.2. As shown in Müller et al. (2010), tidal mixing improves the recirculation of the Labrador Current. By dragging more freshwater into the surface layer of the Labrador Sea, it becomes more stratified which in turn reduces deep convection.

In ER_{pp} the mixed layer depths are to a large extent similar to our reference simulation HR_{pp}. However, in ER_{pp} the convection centre in the Labrador Sea is confined to a more southeastern area with deeper mixed layers, in particular south of Cape Farewell. The deeper mixed layer depths might be related to a stronger doming of isopycnals because of an enhanced cyclonic circulation (or a recirculating Irminger Current) (Pickart et al., 2003; Våge et al., 2011) and to enhanced advection of Labrador Sea water from the Labrador into the Irminger Basin that preconditions the water south of Cape Farewell for convection.

4.5.2 Southern hemisphere

In the Southern Ocean, we define the mixed layer depth as the depth where the density deviates by $0.03\,\mathrm{kg\,m^{-3}}$ from the density at the surface. MPI-ESM1.2 simulates very deep winter mixed layers in the Weddell and Ross Sea (Fig.11). In the Weddell Sea, the convection reaches down into the deep ocean, which is a known problem in many state-of-the-art ESMs (Sallée et al., 2013; Kjellsson et al., 2015; Heuzé et al., 2015; Naughten et al., 2018). Spurious open-ocean deep convection leads to semi-permanent Weddell Sea polynyas, as warm Circumpolar Deep Water is continuously brought to the surface, causing sea ice to melt.

Possible explanations for this widespread bias are: insufficient freshwater input (Kjellsson et al., 2015), in particular glacial melt water (e.g. Stössel et al., 2015), and insufficient wind mixing in summer (Timmermann and Beckmann, 2004). Reduced wind mixing allows salt from brine rejection to accumulate in the winter water layer and eventually to erode the stratification. In both cases, salinity increases in the winter water layer until the weakly stratified water column overturns (Naughten et al., 2018).

The diagnosed mixed layer depth, however, is very sensitive to the chosen density threshold because of the very weakly stratified water column. We decided to apply a commonly used threshold for the Southern Ocean of $\sigma_t = 0.03\,\mathrm{kg\,m^{-3}}$. Note however that if a lower threshold of $\sigma_t = 0.01\,\mathrm{kg\,m^{-3}}$ is chosen, the mixed layer depth rarely exceeds 300 m, because of a shallow stratified surface layer.

Based on two simulations with the GFDL-ESM with different resolutions of their ocean component (0.25° and 0.1°), Dufour et al. (2017) found that deep convection in the Weddell Sea does not necessarily lead to open-ocean polynyas. They argue that excessive vertical mixing in the lower-resolution ocean component hinders the build-up of a heat reservoir at depth that is necessary for Weddell Sea polynyas to occur intermittently as expected under pre-industrial conditions (e.g. de Lavergne et al., 2014; Gordon, 2014). They further argue that the more realistic representation in the higher-resolution simulation stems

Geosci. Model Dev. Discuss., https://doi.org/10.5194/gmd-2018-286
Manuscript under review for journal Geosci. Model Dev.
Discussion started: 17 December 2018

Geoscientific Model Development Discussions

from (1) the fact that mesoscale eddies tend to flatten isopycnals thereby increasing the stratification, and (2) the more detailed bathymetry which allows for a better simulation of dense-water overflows.

Based on forced MPIOM and coupled MPI-ESM simulations with varying resolution, Stössel et al. (2015) found that the surface freshwater flux improves because of better represented Southern Ocean winter sea-ice and water properties with a 0.1° (TP6M) ocean component, and by switching from a forced to a coupled simulation. These findings are consistent with our ER_{pp} simulation (Fig. 11e), where the mixed layer depth in the central Weddell Sea reduces in comparison with HR_{pp} (Fig. 11a). At the same time, the area of deep mixed layers shifts to the eastern part of the Weddell Sea, close to the Maud Rise plateau, where ER_{pp} still simulates very deep mixed layers in September. This, in turn, could be a result of the better resolved bathymetry in this region. Kurtakoti et al. (2018) explained how Maud Rise polynyas formed in a high-resolution (0.1° ocean component) ESM simulation while none in a low-resolution simulation with the same model. A decisive reason for this was the steeper and better resolved bathymetry of and around Maud Rise that allowed for sufficiently strong Taylor columns to form.

As for the larger Weddell Sea polynyas, de Lavergne et al. (2014) and Gordon (2014) argue that such should only emerge under pre-industrial conditions. Even though de Lavergne et al. (2014) praise the low-resolution MPI-ESM for belonging to the class of convecting models, Kurtakoti et al. (2018) explain that large-scale Weddell Sea polynyas should only occur intermittently under pre-industrial conditions and only by growing out from Maud Rise polynyas, which themselves should only occur at high model resolution (0.1°). Since the greenhouse gas forcing of the experiments presented here being fixed at the 1950 level, one would expect the Southern Ocean of the model to already have adjusted to the present-day situation when no Weddell Sea polynyas are expected to occur (due to the southward shift of the precipitation rich westerlies). Strong convection and large Weddell Sea polynyas, as implied by the perpetual large regions of excessively deep mixed layers (Fig. 11), should thus be viewed as an unrealistic behaviour.

As suggested by Timmermann and Beckmann (2004), the vertical mixing scheme affects the sensitivity of spurious deep convection in the Weddell Sea. According to Kjellsson et al. (2015) and Timmermann and Beckmann (2004), sufficient vertical mixing is required in the top 100 m of the mixed layer in the Weddell Sea to prevent polynya formation. However, we chose to reduce the wind induced mixing quadratically with an increased sea ice cover (PP and KPP scheme) in MPI-ESM1.2, which might result in too less mixing under sea ice and thus might also partly explain the deep convection in the Weddell Sea in our simulations. We neglect here that wind induced mixing could increase with increasing sea ice concentration (and could be even larger than for open-ocean conditions), when the momentum flux from the atmosphere to the ocean will be taken over by the ice-ocean stress. Although the KPP scheme reduces the mixed layer depths in the Ross Sea, it enhances deep convection in the central (HR_{kpp}) and in the eastern part of the Weddell Sea (XR_{kpp}). This enhanced deep convection contribute to the enhanced ACC strength in the Drake Passage (Tab. 3), as it causes a steepening of the isopycnals across the ACC and thus an increased geostrophic flow (Jungclaus et al., 2013; Stössel et al., 2015; Naughten et al., 2018).

Besides the resolution of the ocean component and the choice of the vertical ocean mixing scheme, a higher resolution of the atmosphere component has also a distinct effect on the simulated winter mixed layer depth (Fig. 11c versus 11a and Fig. 11d versus 11b), which is related to the reduced meridional pressure gradient (not shown) over the Weddell Sea. Stössel et al. (2015) found an improvement of the high-latitude Southern Ocean water-mass properties and winter sea-ice cover in a

Geosci. Model Dev. Discuss., https://doi.org/10.5194/gmd-2018-286
Manuscript under review for journal Geosci. Model Dev.
Discussion started: 17 December 2018

simulation, where the high-resolution (TP6M) MPIOM was coupled to a T255 atmosphere (ECHAM6) compared to a coupled simulation with a TP6M ocean and T63 atmosphere. In terms of the ocean mixed layer depth, our results support these earlier findings, as also indicated by the reduction of the ACC to more realistic values (Tab. 3).

In all our model simulations shown here, sea-ice salinity has a constant value of $5\,\mathrm{g\,kg^{-1}}$. As explained in Stössel et al. (2015), Vancoppenolle et al. (2009) and Hunke et al. (2011) argue for a sea-ice salinity of about $8\,\mathrm{g\,kg^{-1}}$ for first-year ice, i.e. the kind of sea ice mostly found around Antarctica. Such a higher value would reduce the amount of brine release during ice formation, and thus provide for a more stable upper-ocean water column in fall and winter. Another issue is the ice export from the coast: if too weak, it will strengthen open-ocean convection at the expense of near-boundary convection (e.g. Stössel et al., 2015; Haumann et al., 2016).

4.6 Atlantic meridional overturning circulation

The large-scale global meridional overturning circulation (MOC) is an important carrier of heat and freshwater in the climate system. The Atlantic MOC (AMOC) is considered to be the strongest part of the MOC (Trenberth and Caron, 2001). The North Atlantic contributes about $25\,\%$ of the total poleward heat flux (ocean plus atmosphere) (Srokosz and Bryden, 2015; Lozier et al., 2017). The meridional transport of heat and salt follows the zonally integrated volume transport that, when facing west, emerges a clockwise rotating NADW cell and a counterclockwise rotating Antarctic Bottom Water (AABW) cell.

Fig. 12 shows the associated meridional overturning volume transport stream function, or AMOC, of all 5 simulations, while Tab. 4 shows the time-mean AMOC strength at $26\,^{\circ}\mathrm{N}$ at $1000\,\mathrm{m}$ depth, as well as the heat and salt transports across $50\,^{\circ}\mathrm{N}$. The time-mean of the AMOC is about $14.9\,\mathrm{Sv}$ in $\mathrm{HR_{pp}}$ and comparable to the $16\,\mathrm{Sv}$ of the MPI-ESM1.2-HR described by Müller et al. (2018). It is slightly lower than the observed mean value ($\pm$ one standard deviation) of $17 \pm 4.4\,\mathrm{Sv}$ (Apr 2004 to Feb 2017) from the RAPID array (McCarthy et al., 2015; Smeed et al., 2017). $\mathrm{HR_{kpp}}$ simulates a stronger AMOC of $18.9\,\mathrm{Sv}$, which is the largest value of all our simulations. A possible explanation for this is given below. The volume transport of the overflow waters across the Greenland-Scotland ridge are also slightly higher with the KPP scheme (Tab. 3). After the overflow waters descend along the continental slopes and mix with ambient water masses, they contribute to a stronger NADW cell (Dickson and Brown, 1994) in the KPP simulations.

Figure 12f shows vertical profiles of the AMOC at $26.5\,^{\circ}\mathrm{N}$ in comparison to the RAPID data. All simulations (except $\mathrm{XR_{pp}}$) produce transports close to the observations. The volume transport of $\mathrm{HR_{kpp}}$, however, is on the stronger side of the observations, whereas the transport of the other simulations are on the lower side of the observations. All models show a too strong southward transport of NADW below 2000 m, which suggests a too strong Deep Western Boundary Current.

The reduced wind stress from ECHAM6.3 at T255 results in the above mentioned slowdown of the AMOC in $\mathrm{XR_{pp}}$. In this simulation, the NADW cell reaches a maximum of only about $11.0\,\mathrm{Sv}$, which is slightly higher than the $9.0\,\mathrm{Sv}$ reported by Putrasahan et al. (2018). This discrepancy is because we analyze an earlier period of the same $\mathrm{XR_{pp}}$ simulation when the AMOC is still drifting to lower values. An important finding of this study is that $\mathrm{XR_{kpp}}$, featuring reduced surface winds, results in a similarly strong AMOC of $14.6\,\mathrm{Sv}$ as in $\mathrm{HR_{pp}}$ and $\mathrm{ER_{pp}}$. In terms of volume transport, going to an eddy resolving ocean

Geosci. Model Dev. Discuss., https://doi.org/10.5194/gmd-2018-286
Manuscript under review for journal Geosci. Model Dev.
Discussion started: 17 December 2018

resolution (ER_{pp}) does not increase the strength of the NADW) cell. This finding is opposite to what Hewitt et al. (2016) and Storkey et al. (2018) found.

However, its bottom (AABW) cell becomes stronger (Fig. 12e), which might be because of similar effects as described by Sein et al. (2018), who hypothesize that eddy-induced transport acts to flatten the outcropping isopycnals in the Southern Ocean. So eddies counteract a wind-induced steepening of isopycnals, while at the same time, a stronger vertical gradient between the AABW and the warmer ambient ocean is maintained. The flatter isopycnals reduce the vertical mixing because of a more stratified water column, as indicated by the reduced mixed layer depths in the Weddell Sea in ER (Fig. 11e). Reduced convection maintains denser AABW, seen by sharper gradients of temperature and salinity in ER (Fig. A3e) and it theoretically helps to build up a deep heat reservoir (Dufour et al., 2017) that is required for intermittent Weddell Sea polynyas. However, in our ER simulation, Weddell Sea polynyas still form too frequently. On the other hand, better resolved bathymetry might also be important for the AABW formation over the continental shelves, which is partly resolved in ER.

We define the depth of the NADW cell as the depth where the volume transport crosses the zero line in Fig. 12f. The observed annual mean depth ($\pm$ one standard deviation) of the NADW cell (Tab. 4) from the RAPID data is about $4379 \pm 279\,\mathrm{m}$ at $26.5\,^{\circ}\mathrm{N}$. All our simulations reveal shallower NADW cells of around $3000\,\mathrm{m}$, but with a noticeable tendency to become deeper with the KPP scheme. A stronger AMOC deepens the NADW cell (Marshall et al., 2017), because more NADW is formed by overturning. This is consistent with the mixed layers beeing deeper in the KPP simulations, and with the increased overflow water from the GIN seas (Tab. 3).

In XR_{pp} the NADW cell is shallower ($2665\,\mathrm{m}$), consistent with a much weaker NADW cell. ER_{pp} simulates a slightly deeper ($2941\,\mathrm{m}$) NADW cell than HR_{pp}, probably because of increased overflow water from the GIN seas (Tab. 3), but still not as deep as with the KPP scheme. The higher volume transport of the AMOC with the KPP scheme yields a slightly enhanced heat transport and a considerably higher salt transport across $50\,^{\circ}\mathrm{N}$ (Tab. 4). This larger salt input into the subpolar North Atlantic with KPP is a main reason why the overturning becomes stronger, and in particular why XR_{kpp} maintains a stable AMOC, even under reduced wind forcing.

The stronger deep convection in the northern North Atlantic (Labrador and Irminger Sea) and in the Nordic Seas enhance the local NADW formation that deepens the NADW cell. Note, however, that open-ocean deep convection is not directly associated with a net vertical mass transport (Marotzke and Scott, 1999) and thus the location of convective mixing and of strongest downward mass transfer need not coincide.

The surplus of NADW water has to be replaced by water masses from the NAC, leading to larger volume and salt transports of this current. Once the upper cell in the Atlantic becomes stronger, a positive feedback sets in. A stronger NAC strengthens the cyclonic circulation of the subpolar gyre (Tab. 2) and the separation of water masses in the gyre centres (Labrador/Irminger Sea) from the ambient water masses. This separation of water masses in the gyre centres enhances deep convection because of (1) increased isopycnal doming that leads to a weaker stratification of the water column and to a shallower thermocline, and (2) because of reduced mixing with ambient water, so that the water masses in the gyre centre are exposed longer to the overlaying cold atmosphere, leading to an increased heat loss. Both effects reduce the surface stratification that could be easily eroded,

Geosci. Model Dev. Discuss., https://doi.org/10.5194/gmd-2018-286
Manuscript under review for journal Geosci. Model Dev.
Discussion started: 17 December 2018

which favours deep convection and again strengthens the overturning cell. In addition, increased salt input densifies the upper water masses of the northern North Atlantic and the Nordic Seas, so that convection is enhanced.

As a result of the enhanced AMOC, the adiabatic upwelling branch of the MOC south of the ACC has to become stronger too (Fig. A2). Since KPP uses the same background diffusivities below the mixed layer as with the PP scheme, no significantly different diapycnal diffusion occurs in the Pacific (not shown). That is, the only return pathway is via wind-driven adiabatic upwelling in the Southern Ocean (Marshall and Speer, 2012). An increase in upwelling in the Southern Ocean further strengthens the northern cell (Marshall et al., 2017). This feedback is however acting on longer time scales than the slowdown of the AMOC in our model. Therefore, the Southern Ocean is not the main factor in sustaining a stable AMOC in XR_{kpp}.

5 Summary

We compared control simulations of various MPI-ESM1.2 configurations following the HighResMIP protocol and investigated separately the resolution effects of the atmosphere and ocean model configurations and the effects of an alternative diapycnal ocean mixing scheme on the mean states of the atmosphere and ocean.

5.1 Eddy-resolving ocean

An eddy-resolving ocean reduces biases in the ocean and it has a major impact on the large-scale temperature distribution in the atmosphere. In the atmosphere, the cold biases above the Northern hemisphere were removed, but in particular the cold bias above the ACC. The latter bias could not be removed by just increasing the atmospheric resolution. In the ocean, warm and saline bias in the Southern Atlantic were removed, because of the better representation of the Agulhas Current system (Putrasahan et al., 2015; Cheng et al., 2016) and because of eddy-induced upward transport of fresh and cold water masses, as described in von Storch et al. (2016). In the North Atlantic, the warm and saline bias was removed because of a better simulation of the water properties of the outflowing Mediterranean Water. An eddy-resolving ocean improves the separation of the Gulf Stream, although the NAC remained still too zonal in our simulation. Furthermore, the warm bias of the Atlantic Layer in the Arctic Ocean was removed, probably because of reduced numerical mixing due to the higher resolution, which confirms the results of Wang et al. (2018). Finally, the deep-convection centre shifted to the southeast in the Labrador Sea, and to the east in the Weddell Sea.

5.2 A T255 resolution for the atmosphere

A main improvement with a T255 atmosphere are reduced mixed layer depths in both hemispheres, in particular in the Labrador Sea and in the Weddell Sea. In the Weddell Sea, the ACC transport reduces to realistic values, as reported by Stössel et al. (2015), because of a reduced meridional pressure gradient in the atmosphere across the ACC. Further the reduced pressure gradient above the Weddell Sea reduces the wind forcing of the Weddell Sea polynya. As with an eddy-resolving ocean, the centre of deep convection in the Weddell Sea shifts to the east, to the vicinity of the Maud Rise Plateau. In the northern hemisphere, a T255 atmosphere reduces the near-surface wind speeds over the subpolar gyre. With a reduced wind forcing, the subpolar gyre

slows down and because of less cyclonic movement and less salt advection into the gyre centres, the deep convection reduces (KPP scheme) or completely ceases (PP scheme) with a slowdown of the AMOC, as described by Putrasahan et al. (2018). In contrast to the near-surface, the jet streams became stronger with a T255 atmosphere.

5.3 Effects of the KPP scheme

The main effects of the KPP scheme are stronger deep convection in both hemispheres, as seen by the mixed layer depths. Under convective forcing the non-local fluxes of the KPP scheme produce much higher diffusivities compared with the enhanced diffusivity parameterization that we use for the PP scheme. This stronger deep convection with the KPP scheme produces more local NADW in the convection centres (Labrador, Irminger, and GIN Seas) which in turn strengthens the AMOC. When coupled with the T255 atmosphere, the AMOC remains stable with the KPP scheme because of this enhanced overturning, which produces sufficient NADW to maintain a strong enough upper cell. Another effect of producing deeper mixed layer is a stronger subpolar gyre that domes the isopycnals and helps to precondition the water column for convection. This is also true for the Weddell Gyre with the same effect. The stronger AMOC transports more salt and heat into the North Atlantic, so that the cold bias in the northern hemisphere is removed (except in the upper troposphere).

Code and data availability. The MPI-ESM1.2 model code is made available under a version of the MPI-M Software License Agreement (http://www.mpimet.mpg.de/en/science/models/license). Primary data and scripts used in the analysis, a patch for the MPI-ESM1.2 that contains all modifications we made, and other supplementary information that may be useful in reproducing the author's work are archived by the Max Planck Institute for Meteorology and can be obtained by contacting publications@mpimet.mpg.de.

Author contributions. JJ and JS designed the experiments and DP and KL set up the model configurations and performed the simulations. OG, NB and HH have implemented the new mixing parameterizations in MPIOM. OG prepared the manuscript with contributions from all co-authors.

Competing interests. The authors declare that they have no conflict of interest.

Acknowledgements. We thank the German Computing Centre (DKRZ) for providing the computing resources. This research was funded by the EU Horizon 2020 project PRIMAVERA (grant number 641727). This paper is a contribution to the project S2 (Improved parameterisations and numerics in climate models) of the Collaborative Research Centre TRR 181 "Energy Transfer in Atmosphere and Ocean" funded by the Deutsche Forschungsgemeinschaft (DFG, German Research Foundation) - project number 274762653. JJ acknowledges support by the German BMBF RACE-II project (FKZ 03F0729D). We thank Jürgen Kröger for proofreading the manuscript.

References

Adcroft, A. J., Hill, C., and Marshall, J.: Representation of Topography by Shaved Cells in a Height Coordinate Ocean Model, Mon. Weather Rev., 125, 2293–2315, https://doi.org/10.1175/1520-0493(1997)125<2293:ROTBSC>2.0.CO;2, 1997.

Bacon, S.: Circulation and Fluxes in the North Atlantic between Greenland and Ireland, J. Phys. Oceanogr., 27, 1420–1435, https://doi.org/10.1175/1520-0485(1997)027<1420:CAFITN>2.0.CO;2, 1997.

Bersch, M.: On the circulation of the northeastern North Atlantic, Deep-Sea Res. Pt. I, 42, 1583–1607, https://doi.org/10.1016/0967-0637(95)00071-D, 1995.

Bryden, H. L., Candela, J., and Kinder, T. H.: Exchange through the Strait of Gibraltar, Prog. Oceanog., 33, 201–248, https://doi.org/10.1016/0079-6611(94)90028-0, 1994.

Cheng, Y., Putrasahan, D., Beal, L., and Kirtman, B.: Quantifying Agulhas Leakage in a High-Resolution Climate Model, J. Climate, 29, 6881–6892, https://doi.org/10.1175/JCLI-D-15-0568.1, 2016.

Cheng, Y., Beal, L. M., Kirtman, B. P., and Putrasahan, D.: Interannual Agulhas Leakage Variability and its Regional Climate Imprints, J. Climate, https://doi.org/10.1175/JCLI-D-17-0647.1, 2018.

Clark, R. A.: Transport through the Cape Farewell-Flemish Cap section, Rapp. P. V. Reun. Cons. Int. Explor. Mer., 185, 120–130, 1984.

Cunningham, S. A., Alderson, S. G., King, B. A., and Brandon, M. A.: Transport and variability of the Antarctic circumpolar current in Drake Passage, J. Geophys. Res., 108 (C5), 8084, https://doi.org/10.1029/2001JC001147, 2003.

de Lavergne, C., Palter, J. B., Galbraith, E. D., Bernardello, R., and Marinov, I.: Cessation of deep convection in the open Southern Ocean under anthropogenic climate change, Climate Change, 4, 278–282, https://doi.org/10.1038/nclimate2132, 2014.

Dee, D. P., Uppala, S. M., Simmons, A. J., Berrisford, P., Poli, P., Kobayashi, S., Andrae, U., Balmaseda, M. A., Balsamo, G., Bauer, P., Bechtold, P., Beljaars, A. C. M., van de Berg, L., Bidlot, J., Bormann, N., Delsol, C., Dragani, R., Fuentes, M., Geer, A. J., Haimberger, L., Healy, S. B., Hersbach, H., Hólm, E. V., Isaksen, L., Kåberg, P., Köhler, M., Matricardi, M., McNally, A. P., Monge-Sanz, B. M., Morcrette, J.-J., Park, B.-K., Peubey, C., de Rosnay, P., Tavolato, C., Thépaut, J.-N., and Vitart, F.: The ERA-Interim reanalysis: configuration and performance of the data assimilation system, Q. J. R. Meteorol. Soc., 137, 553–597, https://doi.org/10.1002/qj.828, 2011.

Dengg, J. A., Beckmann, A., and Gerdes, R.: The Warmwatersphere of the North Atlantic Ocean, chap. The Gulf Stream separation problem, pp. 253–290, Gebr. Bornträger, Berlin, 1996.

Dickson, R. R. and Brown, J.: The production of North Atlantic Deep Water: Sources, rates, and pathways, J. Geophys. Res., 99, 12 319–12 341, https://doi.org/10.1029/94JC00530, 1994.

DiMarco, S. F., Chapman, P., Nowlin Jr., W. D., Hacker, P., Donohue, K., Luther, M., Johnson, G. C., and Toole, J.: Volume transport and property distribution of the Mozambique Channel, Deep-Sea Res. II, 49, 1481–1511, https://doi.org/10.1016/S0967-0645(01)00159-X, 2002.

Donohue, K. A., Tracey, K. L., Watts, D. R., Chidichimo, M. P., and Chereskin, T. K.: Mean Antarctic Circumpolar Current transport measured in Drake Passage, Geophys. Res. Lett., 43, 11 760–11 767, https://doi.org/10.1002/2016GL070319, 2016.

Dufour, C. O., Morrison, A. K., Griffies, S. M., Frenger, I., Zanowski, H., and Winton, M.: Preconditioning of the Weddell Sea Polynya by the Ocean Mesoscale and Dense Water Overflows, J. Climate, 30, 7719–7737, https://doi.org/10.1175/JCLI-D-16-0586.1, 2017.

Eyring, V., Bony, S., Meehl, G. A., Senior, C. A., Stevens, B., Stouffer, R. J., and Taylor, K. E.: Overview of the Coupled Model Intercomparison Project Phase 6 (CMIP6) experimental design and organization, Geoscientific Model Development, 9, 1937–1958, https://doi.org/10.5194/gmd-9-1937-2016, 2016.

Fahrbach, E., Meincke, J., Østerhus, S., Rohardt, G., Schauer, U., Tverberg, V., and Verduin, J.: Direct measurements of volume transports through Fram Strait, Polar Research, 20, 217–224, https://doi.org/10.1111/j.1751-8369.2001.tb00059.x, 2006.

Frenger, I., Gruber, R., Knutti, R., and Münnich, M.: Imprint of Southern Ocean eddies on winds, clouds and raindfall, Nat. Geosci., 6, 608–612, https://doi.org/10.1038/ngeo1863, 2013.

Gent, P. R.: A commentary on the Atlantic meridional overturning circulation stability in climate models, Ocean Model., 122, 57–66, https://doi.org/10.1016/j.ocemod.2017.12.006, 2018.

Gent, P. R., Willebrand, J., McDougall, T. J., and McWilliams, J. C.: Parameterizing Eddy-Induced Tracer Transports in Ocean Circulation Models, J. Phys. Oceanogr., 25, 463–474, https://doi.org/10.1175/1520-0485(1995)025<0463:PEITTI>2.0.CO;2, 1995.

Giorgetta, M. A., Jungclaus, J., Reick, C. H., Legutke, S., Bader, J., Böttinger, M., Brovkin, V., Crueger, T., Esch, M., Fieg, K., Glushak, K., Gayler, V., Haak, H., Hollweg, H.-D., Ilyina, T., Kinne, S., Kornblueh, L., Matei, D., Mauritsen, T., Mikolajewicz, U., Mueller, W., Notz, D., Pithan, F., Raddatz, T., Rast, S., Redler, R., Roeckner, E., Schmidt, H., Schnur, R., Segschneider, J., Six, K. D., Stockhause, M., Timmreck, C., Wegner, J., Widmann, H., Wieners, K.-H., Claussen, M., Marotzke, J., and Stevens, B.: Climate and carbon cycle changes from 1850 to 2100 in MPI-ESM simulations for the Coupled Model Intercomparison Project phase 5, J. Adv. Model. Earth Syst., 5, 572–597, https://doi.org/10.1002/jame.20038, 2013.

Good, S. A., Martin, M. J., and Rayner, N. A.: EN4: quality controlled ocean temperature and salinity profiles and monthly objective analyses with uncertainty estimates, J. Geophys. Res., 118, 6704–6716, https://doi.org/10.1002/2013JC009067, 2013.

Gordon, A. L.: Southern Ocean polynya, Nature Clim. Change, 4, 249–250, https://doi.org/10.1038/nclimate2179, 2014.

Gordon, A. L., Sprinthall, J., Van Aken, H. M., Susanto, D., Wijffels, S., Molcard, R., Field, A., Pranowo, W., and Wirasantosa, S.: The Indonesian throughflow during 2004–2006 as observed by the INSTANT program, Dyn. Atmos. Oceans, 50, 115–128, https://doi.org/10.1016/j.dynatnoce.2009.12.002., 2010.

Griffies, S. M., Levy, M., Adcroft, A. J., Danabasoglu, R., Hallberg, R. W., Jacobsen, D., Large, W., and Ringler, T. D.: Theory and numerics of the Community Ocean Vertical Mixing (CVMix) Project, Tech. rep., https://github.com/CVMix/CVMix-description, 2013.

Griffies, S. M. et al.: Coordinated ocean-ice reference experiments (CORES), Ocean Model., 26, 1–46, https://doi.org/10.1016/j.ocemod.2008.08.007, 2009.

Gutjahr, O. and Heinemann, G.: A model-based comparison of extreme winds in the Arctic and around Greenland, Int. J. Climatol., 38, 5272–5292, https://doi.org/10.1002/joc.5729, 2018.

Haarsma, R. J., Roberts, M. J., Vidale, P. L., Senior, C. A., Bellucci, A., Bao, Q., Chang, P., Corti, S., Fučkar, N. S., Guemas, V., von Hardenberg, J., Hazeleger, W., Kodama, C., Koenigk, T., Leung, L. R., Lu, J., Luo, J.-J., Mao, J., Mizielinski, M. S., Mizuta, R., Nobre, P., Satoh, M., Scoccimarro, E., Semmler, T., Small, J., and von Storch, J.-S.: High Resolution Model Intercomparison Project (HighResMIP v1.0) for CMIP6, Geoscientific Model Development, 9, 4185–4208, https://doi.org/10.5194/gmd-9-4185-2016, 2016.

Hagemann, S. and Gates, L. D.: Improving a subgrid runoff parameterization scheme for climae models by the use of a high resolution data derived from satellite observations, Climate Dyn., 21, 349–359, https://doi.org/10.1007/s00382-003-0349-x, 2003.

Hansen, B., Østerhus, S., Turrell, W. R., Jónsson, S., Valdimarsson, H., Hátún, H., and Olsen, S. M.: The Inflow of Atlantic Water, Heat, and Salt to the Nordic Seas Across the Greenland–Scotland Ridge, pp. 15–43, Springer Netherlands, Dordrecht, https://doi.org/10.1007/978-1-4020-6774-7_2, 2008.

Haumann, F. A., Gruber, N., Münnich, M., Frenger, I., and Kern, S.: Sea-ice transport driving Southern Ocean salinity and its recent trends, Nature, 537(7618), 89–92, https://doi.org/10.1038/nature19101, 2016.

Hertwig, E., von Storch, J.-S., Handorf, D., Dethloff, K., Fast, I., and Krismer, T.: Effect of horizontal resolution on ECHAM6-AMIP performance, Clim. Dyn., 45, 185–211, https://doi.org/10.1007/s00382-014-2396-x, 2015.

Heuzé, C., Ridley, J. K., Calvert, D., Stevens, D. P., and Heywood, K. J.: Increasing vertical mixing to reduce Southern Ocean deep convection in NEMO3.4, Geoscientific Model Development, 8, 3119–3130, https://doi.org/10.5194/gmd-8-3119-2015, 2015.

Hewitt, H. T., Roberts, M. J., Hyder, P., Graham, T., Rae, J., Belcher, S. E., et al.: The impact of resolving the Rossby radius at mid-latitudes in the ocean: Results from a high-resolution version of the Met Office GC2 coupled model, Geosci. Model Dev., 9, 3655–3670, https://doi.org/10.5194/gmd-9-3655-2016, 2016.

Holliday, N. P., Bacon, S., Allen, J., and McDonagh, E. L.: Circulation and transport in the western boundary currents at Cape Farewell, Greenland., J. Phys. Oceanogr., 39 (8), 1854–1870, https://doi.org/10.1175/2009JPO4160.1, 2009.

Holloway, G., Dupont, F., Golubeva, E., Haekkinen, S., Hunke, E., Jin, M., Karcher, M., Kauker, F., Maltrud, M., Maqueda, M. A. M., Maslowski, W., Platov, G., Stark, D., Steele, M., Suzuki, T., Wang, J., and Zhang, J.: Water properties and circulation in Arctic Ocean models, Geophys. Res. Oceans, 112, C04S03, https://doi.org/10.1029/2006JC003642, 2007.

Hunke, E. C., Notz, D., Turnker, A. K., and Vancoppenolle, M.: The multiphase physics of sea ice: a review for model developers, Cryosphere, 27, 3784–3801, https://doi.org/10.5194/tc-5-989-2011, 2011.

Ilicak, M., Drange, H., Wang, Q., et al.: An assessment of the Arctic Ocean in a suite of interannual CORE-II simulations. Part III: Hydrography and fluxes, Ocean Model., 100, 141–161, https://doi.org/10.1016/j.ocemod.2016.02.004, 2016.

Imawaki, S., Uchida, H., Ichikawa, H., Fukasawa, M., Umatani, S., and ASUKA Group: Satellite altimeter monitoring the Kuroshio Transport south of Japan, Geophys. Res. Lett., 28, 17–20, https://doi.org/10.1029/2000GL011796, 2001.

Jochumsen, K., Quadfasel, D., Valdimarsson, H., and Jónsson, S.: Variability of the Denmark Strait overflow: Moored time series from 1996–2011, J. Geophys. Res., 117, C12 003, https://doi.org/10.1029/2012JC008244, 2012.

Jochumsen, K., Moritz, M., Nunes, N., Quadfasel, D., Larsen, K. M. H., Hansen, B., Valdimarsson, H., and Jonsson, S.: Revised transport estimates of the Denmark Strait overflow, J. Geophys. Res., 122, 3434–3450, 2017.

Johns, W., Shay, T., Bane, J., and Watts, D.: Gulf Stream structure, transport, and recirculation near 68 ° W, J. Geophys. Res., 100, 817–838, https://doi.org/10.1029/94JC02497, 1995.

Jungclaus, J. H., Fischer, N., Haak, H., Lohmann, K., Marotzke, J., Matei, D., Mikolajewicz, U., Notz, D., and von Storch, J. S.: Characteristics of the ocean simulations in the Max Planck Institute Ocean Model (MPIOM), the ocean component of the MPI-Earth system model, J. Adv. Model. Earth Syst., 5, 422–446, https://doi.org/10.1002/jae.20023, 2013.

Kanzow, T. and Zenk, W.: Structure and transport of the Iceland Scotland Overflow plume along the Reykjanes Ridge in the Iceland Basin, Deep-Sea Res. Pt. I, 86, 82–93, https://doi.org/10.1016/j.dsr.2013.11.003, 2014.

Kanzow, T., Cunningham, S. A., Johns, W. E., Hirschi, J. J.-M., Marotzke, J., Baringer, M. O., Meinen, C. S., Chidichimo, M. P., Atkinson, C., Beal, L. M., Bryden, H. L., and Collins, J.: Seasonal variability of the Atlantic meridional overturning circulation at 26.5 ° N, J. Climate, 23, 5678–5698, https://doi.org/10.1175/2010JCLI3389.1, 2010.

Kjellsson, J., Holland, P. R., Marshall, G. J., Mathiot, P., Aksenov, Y., Coward, A. C., Bacon, S., Megann, A. P., and Ridley, J.: Model sensitivity of the Weddell and Ross seas, Antarctica, to vertical mixing and freshwater forcing, Ocean Modelling, 94, 141–152, https://doi.org/10.1016/j.ocemod.2015.08.003, 2015.

Kurtakoti, P., Veneziani, M., Stössel, A., and Weijer, W.: Preconditioning and Formation of Maud Rise Polynyas in a High-Resolution Earth System Model, J. Climate, https://doi.org/10.1175/JCLI-D-18-0392.1, 2018.

Large, W. G., McWilliams, J. C., and Doney, S. C.: Oceanic vertical mixing: A review and a model with a nonlocal boundary layer parameterization, Rev. Geophys., 21, 363–403, https://doi.org/10.1029/94RG01872, 1994.

Lherminier, P., Mercier, H., Gourcuff, C., Alvarez, M., Bacon, S., and Kermabon, C.: Transports across the 2002 Greenland-Portugal Ovide section and comparison with 1997, J. Geophys. Res., 112, C07 003, https://doi.org/10.1029/2006JC003716, 2007.

Liu, X., Chang, P., Kurian, J., Saravan, R., and Lin, X.: Satellite-Observed Precipitation Response to Ocean Mesoscale Eddies, J. Climate, 31, 6879–6895, https://doi.org/10.1175/JCLI-D-17-0668.1, 2018.

Lozier, M. S. et al.: Overturning in the Subpolar North Atlantic Program: A new international ocean observing system, Bull. Am. Meteorol. Soc., 98, 43–63, https://doi.org/10.1175/BAMS-D-16-0057.1, 2017.

Ma, X., Jing, Z., Chang, P., Liu, X., Montuoro, R., Small, J. R., Bryan, F. O., Greatbatch, R. J., Brandt, P., Wu, D., Lin, X., and Wu, L.: Western boundary currents regulated by the interaction between ocean eddies and the atmosphere, Nature, 535, 533–537, https://doi.org/10.1038/nature18640, 2016.

Marotzke, J. and Scott, J. R.: Convective Mixing and the Thermohaline Circulation, J. Phys. Oceanogr., 29, 2962–2970, https://doi.org/10.1175/1520-0485(1999)029<2962:CMATTC>2.0.CO;2, 1999.

Marshall, J. and Speer, K.: Closure of the meridional overturning circulation through Southern Ocean upwelling, Nat. Geosci., 5 (3), 171–180, https://doi.org/10.1038/ngeo1391, 2012.

Marshall, J., Scott, J. R., Romanou, A., Kelley, M., and Leboissetier, A.: The dependence of the ocean's MOC on mesoscale eddy diffusivities: A model study, Ocean Model., 111, 1–8, 2017.

Marsland, S. J., Haak, H., Jungclaus, J. H., Latif, M., and Röske, F.: The Max Planck Institute global ocean/sea ice model with orthogonal curvilinear coordinates, Ocean Model., 5, 91–127, 2003.

Mauritsen, T., Stevens, B., Roeckner, E., Crueger, T., Esch, M., Giorgetta, M., Haak, H., Jungclaus, J. H., Klocke, D., Matei, D., Mikolajewicz, U., Notz, D., Pincus, R., Schmidt, H., and Tomassini, L.: Tuning the climate of a global model, J. Adv. Model. Earth Syst., 4(3), M00A01, https://doi.org/10.1029/2012MS000154, 2012.

Mauritsen, T. et al.: Developments in the MPI-M Earth System Model version 1.2 (MPI-ESM1.2) and its response to increasing CO2, J. Adv. Model. Earth Syst., submitted, 2018.

McCarthy, G. D., Smeed, D. A., Johns, W. E., Frajka-Williams, E., Moat, B. I., Rayner, D., Baringer, M. O., Meinen, C. S., Collins, J., and Bryden, H. L.: Measuring the Atlantic Meridional Circulation at 26°N, Prog. in Ocean., 130, 91–111, https://doi.org/10.1016/j.pocean.2014.10.006, 2015.

McClean, J. L., Bader, D. C., Bryan, F. O., Maltrud, M. E., Dennis, J. M., Mirin, A. A., Jones, P. W., Kim, Y. Y., Ivanova, D. P., Vertenstein, M., Boyle, J. S., Jacob, R. L., Norton, N., Craig, A., and Worley, P. H.: A prototype two-decade fully-coupled fine-resolution CCSM simulation, Ocean Model., 39, 10–30, https://doi.org/10.1016/j.ocemod.2011.02.011, 2011.

McDonagh, E. L., King, B. A., Bryden, H. L., Courtois, P., Szuts, Z., Baringer, M., Cunningham, S. A., Atkinson, C., and McCarthy, G.: Continuous estimate of Atlantic Oceanic freshwater flux at 26.5 °N, J. Climate, 28, 8888–8906, https://doi.org/10.1175/JCLI-D-14-00519.1, 2015.

Meredith, M. P., Woodworth, P. L., Chereskin, T. K., Marshall, D. P., Allison, L. C., Bigg, G. R., Donohue, K., Heywood, K. J., Hughes, C. W., Hibbert, A., Hogg, A. M., Johnson, H. L., Loïc, J., King, B. A., Leach, H., Lenn, Y.-D., Morales Maqueda, M. A., Munday, D. R., Naveira Garabato, A. C., Provost, C., Sallée, J.-B., and Sprintall, J.: Sustained monitoring of the Southern Ocean at Drake Passage: Past achievements and future priorities, Rev. Geophys., 49, RG4005, https://doi.org/10.1029/2010RG000348, 2011.

Milinski, S., Bader, J., Haak, H., Siongco, A. C., and Jungclaus, J. H.: High atmospheric horizontal resolution eliminates the wind-driven coastal warm bias in the southeastern tropical Atlantic, Geophys. Res. Lett., 43, 10 455–10 462, https://doi.org/10.1002/2016GL070530, 2016GL070530, 2016.

Müller, M., Haak, H., Jungclaus, J. H., Sündermann, J., and Thomas, M.: The effect of ocean tides on a climate model simulation, Ocean Model., 35, 304–313, 2010.

Müller, W. A., Jungclaus, J. H., Mauritsen, T., Baehr, J., Bittner, M., Budich, R., Bunzel, F., Esch, M., Ghosh, R., Haak, H., Ilyina, T., Kleine, T., Kornblueh, L., Li, H., Modali, K., Notz, D., Pohlmann, H., Roeckner, E., Stemmler, I., Tian, F., and Marotzke, J.: A higher-resolution version of the Max Planck Institute Earth System Model (MPI-ESM 1.2-HR), J. Adv. Model. Earth Syst., 9, https://doi.org/10.1029/2017MS001217, 2018.

Naughten, K., Meissner, K. J., Galton-Fenzi, B. K., England, M. H., Timmermann, R., Hellmer, H. H., Hattermann, T., and Debernard, J. B.: Intercomparison of Antarctic ice-shelf, ocean, and sea-ice interactions simulated by MetROMS-iceshelf and FESOM 1.4, Geosci. Model. Dev., 11, 1257–1292, https://doi.org/10.5194/gmd-11-1257-2018, 2018.

Notz, D., Haumann, F. A., Haak, H., Jungclaus, J. H., and Marotzke, J.: Arctic sea-ice evolution as modeled by Max Planck Institute for Meteorology's Earth system model, J. Adv. Model. Earth Syst., 5, 173–194, https://doi.org/10.1002/jame.20016, 2013.

Nowlin Jr., W. D. and Klinck, J. M.: The physics of the Antarctic Circumpolar Current, Rev. Geophys., 24(3), 469–491, https://doi.org/10.1029/RG024i003p00469, 1986.

Pacanowski, R. C. and Philander, S. G. H.: Parameterization of Vertical Mixing in Numerical Models of Tropical Oceans, J. Phys. Oceanogr., 11, 1443–1451, https://doi.org/10.1175/1520-0485(1981)011<1443:POVMIN>2.0.CO;2, 1981.

Pickart, R. S., Spall, M. A., Ribergaard, M. H., Moore, G. W. K., and Milliff, R. F.: Deep convection in the Irminger Sea forced by the Greenland tip jet, Nature, 424, 152–156, https://doi.org/10.1038/nature01729, 2003.

Putrasahan, D., Kirtman, B. P., and Beal, L. M.: Modulation of SST Interannual Variability in the Agulhas Leakage Region Associated with ENSO, J. Climate, 29, 7089–7102, https://doi.org/10.1175/JCLI-D-15-0172.1, 2016.

Putrasahan, D. A., Miller, A. J., and Seo, H.: Regional coupled ocean–atmosphere downscaling in the Southeast Pacific: impacts on upwelling, mesoscale air–sea fluxes, and ocean eddies, Ocean Dyn., 63, 463–488, https://doi.org/10.1007/s10236-013-0608-2, 2013.

Putrasahan, D. A., Beal, L. M., Kirtman, B. P., and Cheng, Y.: A new Eulerian method to estimate "spicy" Agulhas leakage in climate models, J. Climate, 42, 4532–4539, https://doi.org/10.1002/2015GL064482, 2015.

Putrasahan, D. A., Lohmann, K., von Storch, J. S., Jungclaus, J. H., Haak, H., and Gutjahr, O.: Surface flux drivers for the slowdown of the Atlantic Meridional Overturning Circulation in a high-resolution global coupled climate model, J. Adv. Model. Earth Syst., in preparation, 2018.

Redi, M. H.: Oceanic Isopycnal Mixing by Coordinate Rotation, Journal of Physical Oceanography, 12, 1154–1158, https://doi.org/10.1175/1520-0485(1982)012<1154:OIMBCR>2.0.CO;2, 1982.

Reick, C., Raddatz, T., Brovkin, V., and Gayler, V.: Representatoin of natural and anthropogenic land cover changes in MPI-ESM, J. Adv. Model. Earth Syst., 5, 459–482, https://doi.org/10.1002/jame.20022, 2013.

Ridderinkhof, H., van der Werf, P. M., Ullgren, J. E., van Aken, H. M., van Leeuwen, P. J., and de Ruijter, P. M.: Seasonal and interannual variability in the Mozambique Channel from moored current observations, J. Geophys. Res., 115, C06 010, https://doi.org/10.1029/2009JC005619, 2010.

Rossby, T. and Flagg, C.: Direct measurement of volume flux in the Faroe-Shetland Channel and over the Iceland-Faroe Ridge, Geophys. Res. Lett., 39, L07 602, https://doi.org/10.1029/2012GL051269, 2012.

Sallée, J.-B., Shuckburgh, E., Bruneau, N., Meijers, A. J. S., Bracegirdle, T. J., and Wang, Z.: Assessment of Southern Ocean mixed-layer depths in CMIP5 models: Historical bias and forcing response, J. Geophys. Res. Oceans, 118, 1845–1862, https://doi.org/10.1002/jgrc.20157, 2013.

Schweiger, A., Lindsay, R., Zhang, J., Steele, M., Stern, H., and Kwok, R.: Uncertainty in modelled Arctic sea ice volume, J. Geophys. Res. Oceans, 116, D06, https://doi.org/10.1029/2011JC007084, 2011.

Sein, D. V., Koldunov, N. V., Danilov, S., Sidorenko, D., Wekerle, C., Cabos, W., Rackow, T., Scholz, P., Semmler, T., Wang, Q., and Jung, T.: The relative influence of atmospheric and oceanic model resolution on the circulation of the North Atlantic Ocean in a coupled climate model, J. Adv. Model. Earth Syst., 100, https://doi.org/10.1029/2018MS001327, 2018.

Small, R. J., Curchitser, E., Hedstrom, K., Kauffmann, B., and Large, W. G.: The Benguela Upwelling System: Quantifying the Sensitivity to Resolution and Coastal Wind Representation in a Global Climate Model, J. Climate, 28, 9409–9432, https://doi.org/10.1175/JCLI-D-15-0192.1, 2015.

Smeed, D., McCarthy, G., Rayner, D., Moat, B. I., Johns, W. E., Baringer, M. O., and Meinen, C. S.: Atlantic meridional overturning circulation observed by the RAPID-MOCHA-WBTS (RAPID-Meridional Overturning Circulation and Heatflux Array-Western Boundary Time Series) array at 26N from 2004 to 2017. British Oceanographic Data Centre - Natural Environment Research Council, UK, https://doi.org/10.5285/5acfd143-1104-7b58-e053-6c86abc0d94b, 2017.

Soto-Navarro, J., Criado-Aldeanueva, F., García-Lafuente, J., and Sánchez-Román, A.: Estimation of the Atlantic inflow through the Strait of Gibraltar from climatological and in situ data, J. Geophys. Res., 115, C10 023, https://doi.org/10.1029/2010JC006302, 2010.

Srokosz, M. A. and Bryden, H. L.: Observing the Atlantic Meridional Overturning Circulation yields a decade of inevitable surprises, Science, 348(6241), 1255 575, https://doi.org/10.1126/science.1255575, 2015.

Stevens, B., Giorgetta, M., Esch, M., Mauritsen, T., Crueger, T., Rast, S., Salzmann, M., Schmidt, H., Bader, J., Block, K., Brokopf, R., Fast, I., Kinne, S., Kornblueh, L., Lohmann, U., Pincus, R., Reichler, T., and Roeckner, E.: Atmospheric component of the MPI-M Earth System Model: ECHAM6, J. Adv. Model. Earth Syst., 5, 146–172, https://doi.org/10.1002/jame.20015, 2013.

Storkey, D., Blaker, A. T., Mathiot, P., Megann, A., Aksenov, Y., Blockley, E. W., et al.: UK Global Ocean GO6 and GO7: A traceable hierarchy of model resolutions, Geosci. Model Dev, 11, 3187–3213, https://doi.org/10.5194/gmd.11-3187-2018, 2018.

Stössel, A., Notz, D., Haumann, F. A., Haak, H., Jungclaus, J., and Mikolajewicz, U.: Controlling high-latitude Southern Ocean convection in climate models, Ocean Model., 86, 58–75, https://doi.org/10.1016/j.ocemod.2014.11.008, 2015.

Stössel, A., von Storch, J., Notz, D., Haak, H., and Gerdes, R.: High-frequency and meso-scale winter sea-ice variability in the Southern Oscillation in a high resolution global ocean model, Ocean Dyn., https://doi.org/10.1007/s10236-018-1135-y, 2018.

Timmermann, R. and Beckmann, A.: Parameterization of vertical mixing in the Weddell Sea, Ocean Model., 6, 83–100, https://doi.org/10.1016/S1463-5003(02)00061-6, 2004.

Toggweiler, J. R. and Samuels, B.: Effect of Drake Passage on the global thermohaline circulation, Deep-Sea Res. I, 42, 477–500, https://doi.org/10.1016/0967-0637(95)00012-U, 1995.

Trenberth, K. E. and Caron, J. M.: Estimates of merional atmosphere and ocean heat transports, J. Climate, 14, 3433–3443, https://doi.org/10.1175/1520-0442(2001)014<3433:EOMAAO>2.0.CO;2, 2001.

Våge, K., Pickart, R. S., Moore, G. W. K., and Ribergaard, M. H.: Winter Mixed Layer Development in the Central Irminger Sea: The Effect of Strong, Intermittent Wind Events, J. Phys. Oceanogr., 38, 541–565, https://doi.org/10.1175/2007JPO3678.1, 2008.

Våge, K., Pickart, R., Sarafanov, A., Knutsen, Ø., Mercier, H., Lherminier, P., van Aken, H. M., Meincke, J., Quadfasel, D., and Bacon, S.: The Irminger Gyre: circulation, convection, and interannual veriability, Deep-Sea Res. I, 58, 590–614, https://doi.org/10.1016/j.dsr.2011.03001, 2011.

Valcke, S.: The OASIS3 coupler: a European climate modelling community software, Geosci. Model. Dev., 6, 373–388, https://doi.org/10.5194/gmd-6-373-2013, 2013.

Vancoppenolle, M., Fichefet, T., and Goosse, H.: Simulating the mass balance and salinity of Arctic and Antarctic sea ice. 2: Importance of sea ice salinity variations, Ocean. Modell., 27, 54–69, https://doi.org/10.1016/j.ocemod.2008.11.003, 2009.

von Storch, J.-S., Eden, C., Fast, I., Haak, H., Hernández-Deckers, D., Maier-Reimer, E., Marotzke, J., and Stammer, D.: An Estimate of the Lorenz Energy Cycle for the World Ocean Based on the STORM/NCEP Simulation, J. Phys. Oceanogr., 42, 2185–2205, https://doi.org/10.1175/JPO-D-12-079.1, 2012.

von Storch, J. S., Haak, H., Hertwig, E., and Fast, I.: Vertical heat and salt fluxes due to resolved and parameterized meso-scale Eddies, Ocean Model., 108, 1–19, https://doi.org/10.1016/j.ocemod.2016.10.001, 2016.

Wang, Q., Danilov, S., Sidorenko, D., Timmermann, R., Wekerle, C., Wang, X., Jung, T., and Schröter, J.: The Finite Element Sea Ice-Ocean Model FESOM v.1.4: formulation of an ocean general circulation model, Geosci. Model. Dev., 7, 663–693, https://doi.org/10.5194/gmd-7-663-2014, 2014.

Wang, Q., Wekerle, C., Danilov, S., Wang, X., and Jung, T.: A 4.5 km resolution Arctic Ocean simulation with the global multi-resolution model FESOM1.4, Geosci. Model Dev., 11, 1229–1255, https://doi.org/10.5194/gmd-11-1229-2018, 2018.

Wolff, J. O., Maier-Reimer, E., and Legutke, S.: The Hamburg Ocean Primitive Equation Model HOPE, Tech. Rep. 13, German Climate Computer Center (DKRZ), 1997.

Woodgate, R., Weingartner, T., and Lindsa, R.: Observed increases in Bering Strait oceanic fluxes from the Pacific to the Arctic from 2001 to 2011 and their impacts on the Arctic Ocean water column, Geophys. Res. Lett., 39, L24 603, https://doi.org/10.1029/2012GL054092, 2012.

Woodgate, R. A., Aagard, K., and Weingartner, T. J.: Interannual changes in the Bering Strait fluxes of volume, heat, and freshwater between 1991 and 2004, Geophys. Res. Lett., 33, L15 609, https://doi.org/10.1029/2006GL02693., 2006.

Zhang, J. and Rothrock, D. A.: Modeling Global Sea Ice with a Thickness and Enthalpy Distribution Model in Generalized Curvilinear Coordinates, Mon. Weather Rev., 131, 845–861, https://doi.org/10.1175/1520-0493(2003)131<0845:MGSIWA>2.0.CO;2, 2003.

Zhang, J. and Steele, M.: Effect of vertical mixing on the Atlantic Water layer circulation in the Arctic Ocean, Geophys. Res. Oceans, 112, C04S04, https://doi.org/10.1029/2006JC003732, 2007.

Geosci. Model Dev. Discuss., https://doi.org/10.5194/gmd-2018-286
Manuscript under review for journal Geosci. Model Dev.
Discussion started: 17 December 2018

Geoscientific Model Development Discussions
Open Access
EGU

Table 1. Overview of MPI-ESM1.2 control simulations used within this study and their horizontal resolutions. The number of vertical levels are 95 in the atmosphere and 40 in the ocean, respectively. In brackets, the nominal horizontal resolution in a Gaussian grid (approximated at the equator) is given. All models use 30 years of spin-up and are analysed for the subsequent 50 years.

Name	Atmosphere resolution	Ocean resolution	Diapycnal mixing scheme
HR	T127 (0.93° or ~103 km)	TP04 (0.4° or ~44 km)	PP, KPP
XR	T255 (0.46° or ~51 km)	TP04 (0.4° or ~44 km)	PP, KPP
ER	T127 (0.93° or ~103 km)	TP6M (0.1° or ~11 km)	PP

Geosci. Model Dev. Discuss., https://doi.org/10.5194/gmd-2018-286
Manuscript under review for journal Geosci. Model Dev.
Discussion started: 17 December 2018

Geoscientific Model Development Discussions
Open Access
EGU

Table 2. Maximum values of barotropic stream function (gyre strengths) in Sverdrup ($\mathrm{Sv} := 10^6\,\mathrm{m}^3\,\mathrm{s}^{-1}$) simulated by MPI-ESM1.2 and from observations.

Region	HR_{pp}	HR_{kpp}	XR_{pp}	XR_{kpp}	ER_{pp}	Obs.	Reference
Subpolar gyre (North Atlantic)	34.6	40.6	31.0	32.1	36.6	26.0 to 40.0	Clark (1984); Bersch (1995); Bacon (1997); Lherminier et al. (2007); Holliday et al. (2009)
Subtropical gyre (North Atlantic)	48.2	64.9	44.0	63.9	62.8	46.0 to 61.0	Johns et al. (1995)
Subtropical gyre (Pacific)	84.1	116.3	73.6	95.5	80.7	42.0±2.5	Imawaki et al. (2001)

Geosci. Model Dev. Discuss., https://doi.org/10.5194/gmd-2018-286
Manuscript under review for journal Geosci. Model Dev.
Discussion started: 17 December 2018

Geoscientific Model Development Discussions

Table 3. Simulated (mean ± one standard deviation) and observed net volume transports ($\mathrm{Sv} := 10^6\,\mathrm{m}^3\,\mathrm{s}^{-1}$) across sections.

Section	HR_{pp}	HR_{kpp}	XR_{pp}	XR_{kpp}	ER_{pp}	Obs.	Reference
Bering Strait	0.7 ± 0.1	0.7 ± 0.1	0.5 ± 0.1	0.6 ± 0.1	0.9 ± 0.1	0.8 [0.7 to 1.1]	Woodgate et al. (2006, 2012)
Fram Strait	2.5 ± 0.6	1.9 ± 0.4	2.5 ± 0.6	1.9 ± 0.5	1.0 ± 0.4	4.2 ± 2.3	Fahrbach et al. (2006)
Denmark Strait	3.9 ± 0.6	4.2 ± 0.7	4.1 ± 0.6	3.9 ± 0.7	4.6 ± 0.4	4.6	Hansen et al. (2008)
						3.4 ± 1.4	Jochumsen et al. (2012)
						3.2 ± 0.5	Jochumsen et al. (2017)
Iceland – Scotland	4.0 ± 0.8	5.0 ± 1.0	4.2 ± 0.8	4.4 ± 1.0	5.5 ± 0.6	4.8	Hansen et al. (2008)
						4.6 ± 0.25	Rossby and Flagg (2012)
						3.8 ± 0.6	Kanzow and Zenk (2014)
Florida Current	14.6 ± 0.7	15.5 ± 0.7	12.4 ± 0.6	14.1 ± 0.6	24.7 ± 0.8	31.7	Kanzow et al. (2010)
						31.6 ± 2.7	McDonagh et al. (2015)
Strait of Gibraltar	0.04 ± 0.01	0.04 ± 0.01	0.04 ± 0.01	0.04 ± 0.01	0.05 ± 0.01	0.038 ± 0.007	Soto-Navarro et al. (2010)
						0.041	Bryden et al. (1994)
Indonesian Throughflow	8.5 ± 0.8	9.5 ± 0.9	8.0 ± 0.5	8.5 ± 0.8	13.0 ± 0.8	11.6 to 15.7	Gordon et al. (2010)
Mozambique Channel	8.8 ± 1.7	6.5 ± 2.0	8.0 ± 1.3	5.3 ± 1.9	13.6 ± 1.2	5.0 to 26.0	DiMarco et al. (2002)
						16.7 ± 8.9	Ridderinkhof et al. (2010)
Drake Passage	161.7 ± 3.0	191.9 ± 2.6	150.1 ± 4.1	170.2 ± 3.0	140.9 ± 3.0	134.0 ± 14.0	Nowlin Jr. and Klinck (1986)
						137.0 ± 8.0	Cunningham et al. (2003)
						136.7 ± 6.9	Meredith et al. (2011)
						173.3 ± 10.7	Donohue et al. (2016)

Geosci. Model Dev. Discuss., https://doi.org/10.5194/gmd-2018-286
Manuscript under review for journal Geosci. Model Dev.
Discussion started: 17 December 2018

Geoscientific Model Development Discussions
Open Access
EGU

Table 4. Time-mean AMOC volume transports (± one standard deviation of annual means) at $26\,^{\circ}\mathrm{N}$ in 1000 m depth simulated by MPI-ESM1.2 and the depth of the North Atlantic Deep Water (NADW) cell at $26.5\,^{\circ}\mathrm{N}$ (defined where the stream function crosses zero). The observed annual mean (± on standard deviation) NADW cell depth from the RAPID-MOCHA-WBTS array (Smeed et al., 2017) is $4379 \pm 279\,\mathrm{m}$. Further, the time-mean (± one standard deviation of annual means) heat and salt transports across $50\,^{\circ}\mathrm{N}$ are shown (positive means northward transport).

Property	HR_{pp}	HR_{kpp}	XR_{pp}	XR_{kpp}	ER_{pp}
AMOC volume (Sv)	14.9 ± 3.5	18.9 ± 4.0	11.0 ± 3.8	14.6 ± 3.9	14.9 ± 3.6
NADW cell depth (m)	2865 ± 270	3176 ± 334	2665 ± 287	2979 ± 489	2941 ± 265
Atl. heat transport across $50\,^{\circ}\mathrm{N}$ (PW)	0.60 ± 0.04	0.63 ± 0.06	0.42 ± 0.06	0.52 ± 0.05	0.57 ± 0.03
Atl. salt transport across $50\,^{\circ}\mathrm{N}$ ($10^6\,\mathrm{kg\,s^{-1}}$)	0.28 ± 1.89	0.64 ± 2.18	-1.04 ± 2.54	0.4 ± 2.11	-0.22 ± 1.27

Geosci. Model Dev. Discuss., https://doi.org/10.5194/gmd-2018-286
Manuscript under review for journal Geosci. Model Dev.
Discussion started: 17 December 2018

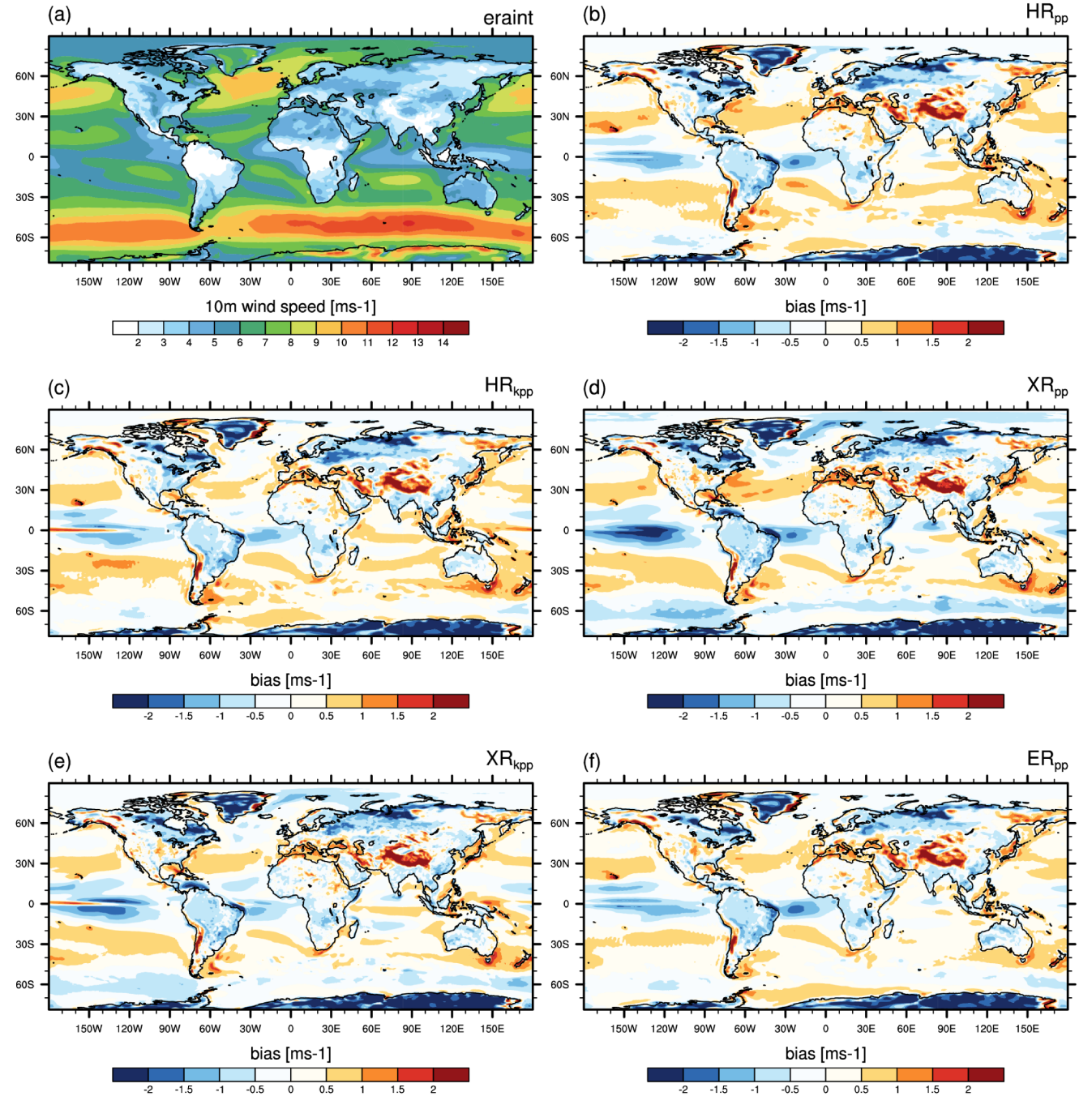

Figure 1. Annual mean 10 m wind speed from (a) ERA-Interim (1979–2005) and the bias of: (b) HR_{pp}, (c) HR_{kpp}, (d) XR_{pp}, (e) XR_{kpp}, and (f) ER_{pp}.

Geosci. Model Dev. Discuss., https://doi.org/10.5194/gmd-2018-286
Manuscript under review for journal Geosci. Model Dev.
Discussion started: 17 December 2018

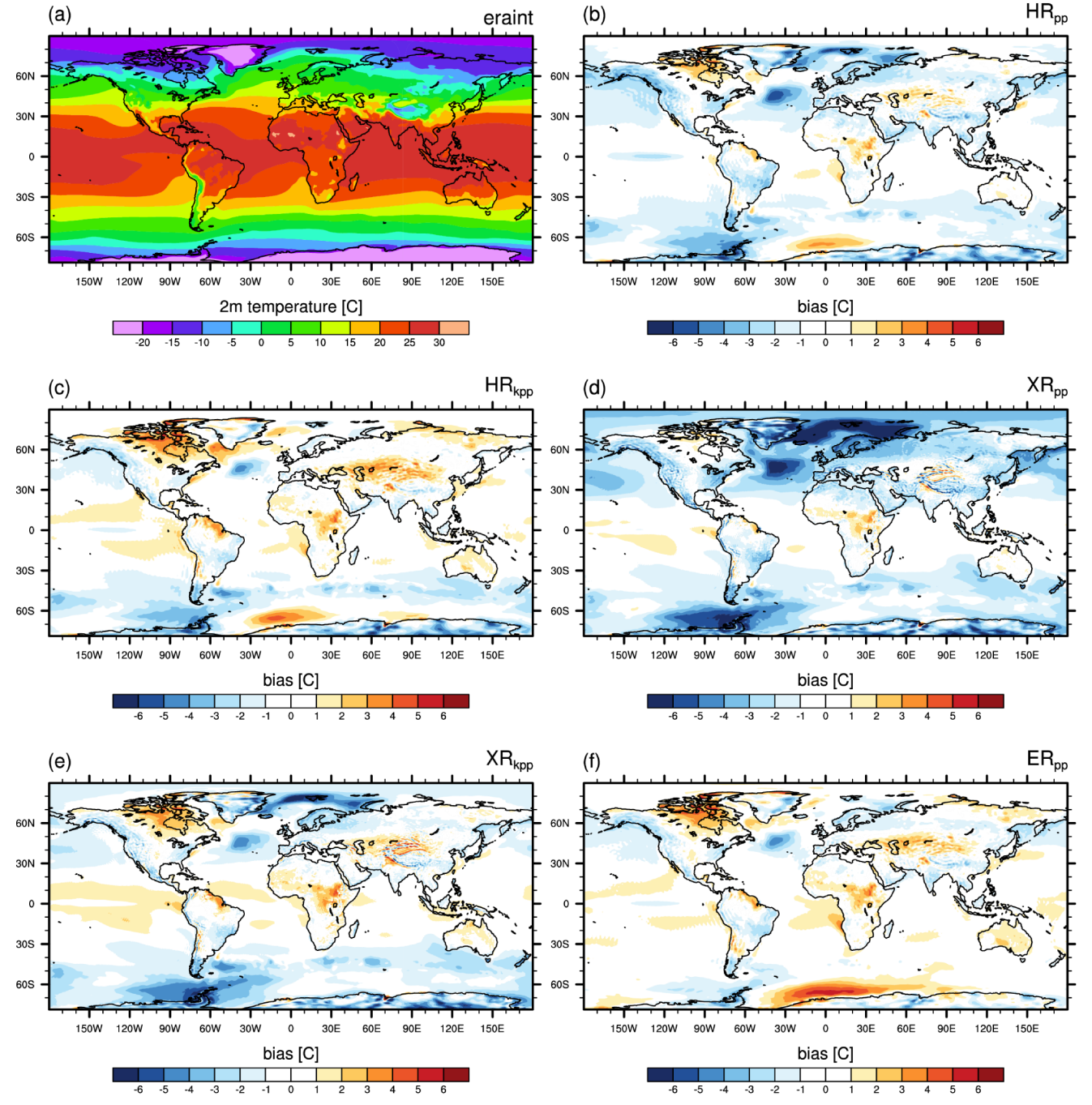

Figure 2. Annual mean 2 m temperature from (a) ERA-Interim (1979–2005) and the bias of: (b) HR_{pp}, (c) HR_{kpp}, (d) XR_{pp}, (e) XR_{kpp}, and (f) ER_{pp}.

Geosci. Model Dev. Discuss., https://doi.org/10.5194/gmd-2018-286
Manuscript under review for journal Geosci. Model Dev.
Discussion started: 17 December 2018

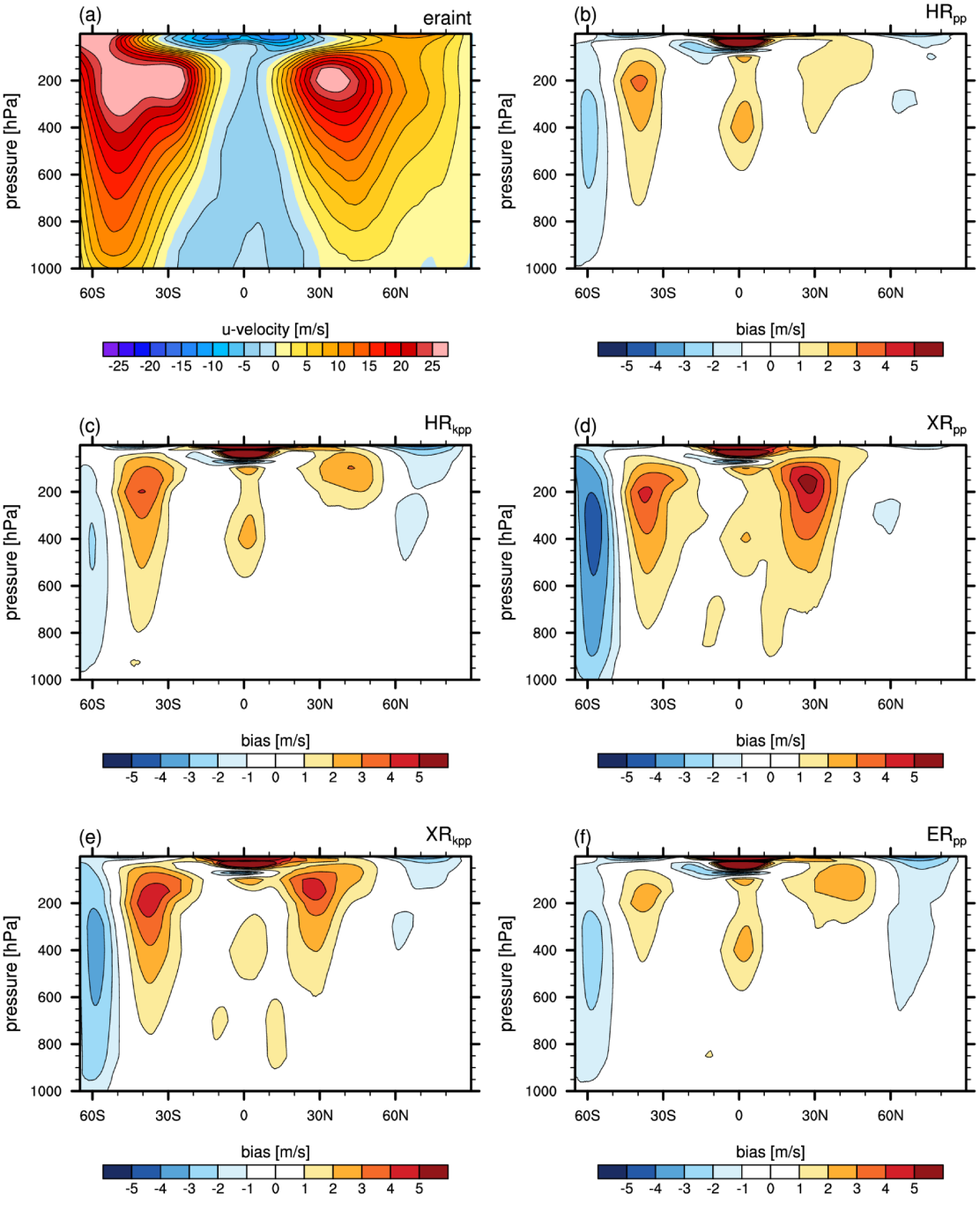

Figure 3. Global zonally-averaged u-velocity from (a) ERA-Interim (1979–2005) and the bias (MPI-ESM1.2 minus ERA-Interim) of: (b) HR_{pp}, (c) HR_{kpp}, (d) XR_{pp}, (e) XR_{kpp}, and (f) ER_{pp}.

Geosci. Model Dev. Discuss., https://doi.org/10.5194/gmd-2018-286
Manuscript under review for journal Geosci. Model Dev.
Discussion started: 17 December 2018

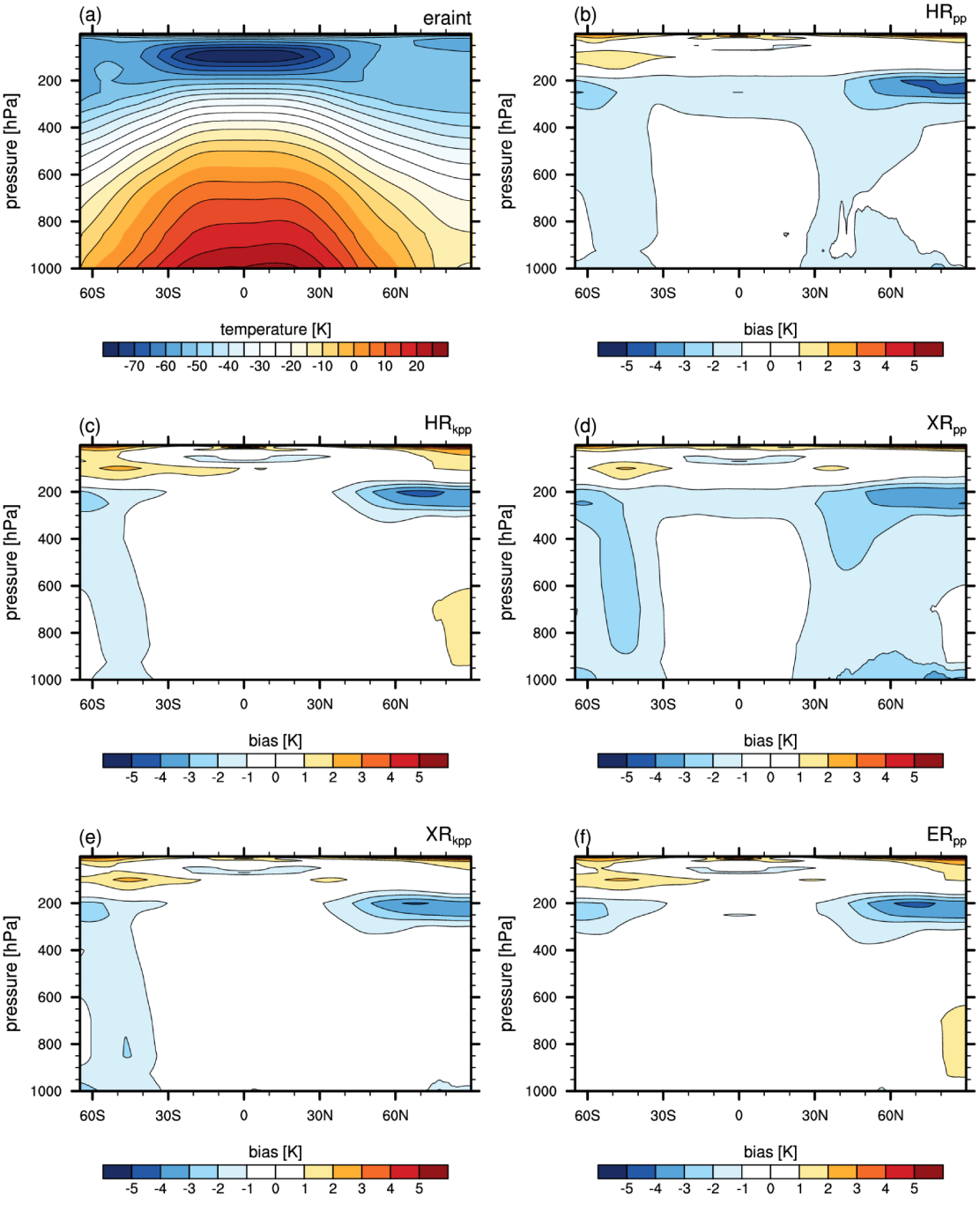

Figure 4. Global zonally-averaged temperature from (a) ERA-Interim (1979–2005) and the bias (MPI-ESM1.2 minus ERA-Interim) of (b) HR_{pp}, (c) HR_{kpp}, (d) XR_{pp}, (e) XR_{kpp}, and (f) ER_{pp}.

Geosci. Model Dev. Discuss., https://doi.org/10.5194/gmd-2018-286
Manuscript under review for journal Geosci. Model Dev.
Discussion started: 17 December 2018

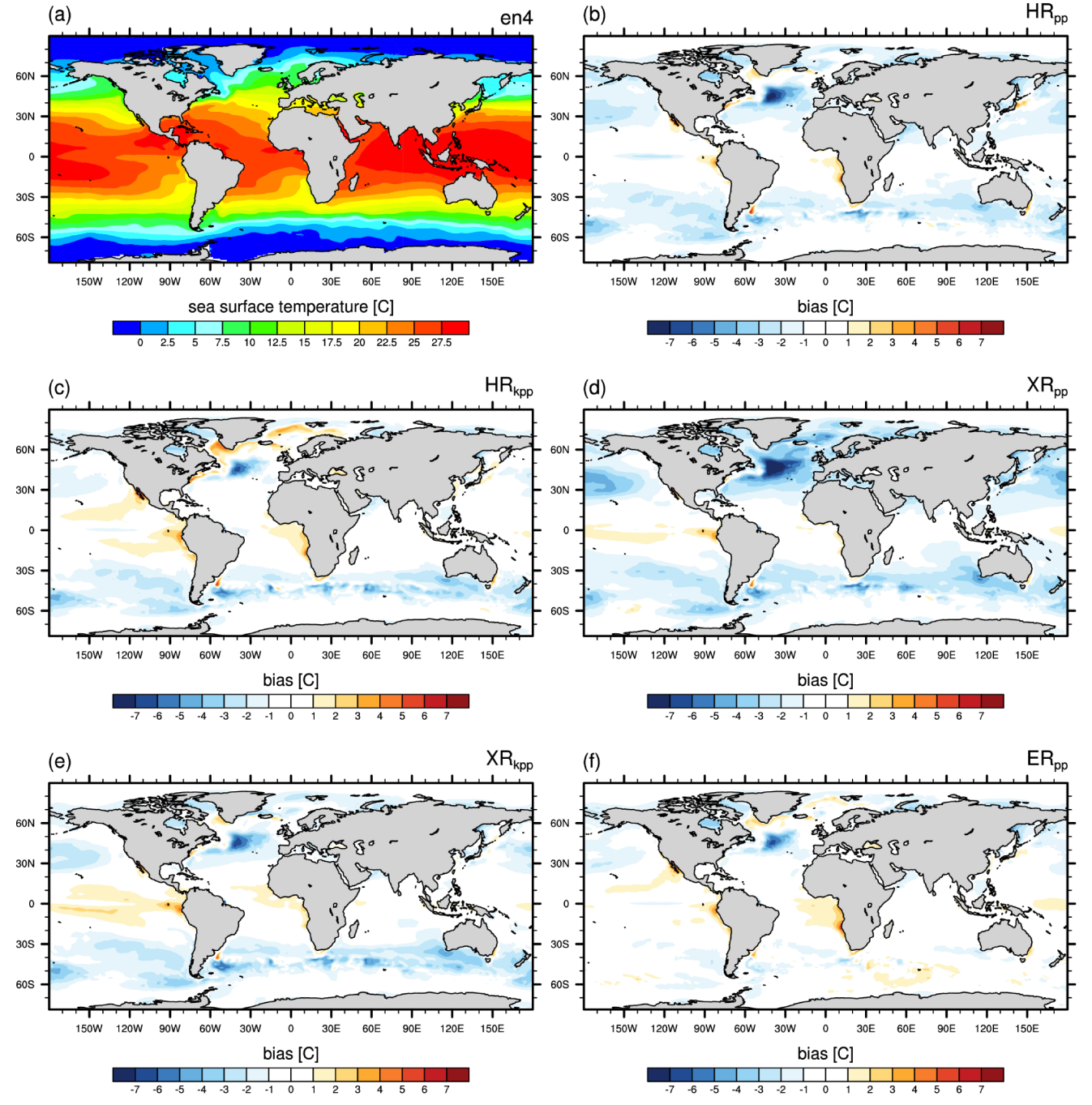

Figure 5. Sea surface temperature (°C) from (a) EN4 (averaged over 1945–1955) and differences: MPI-ESM1.2 minus EN4 for (b) HR_{pp},(c) HR_{kpp}, (d) XR_{pp}, and (e) XR_{kpp}, and (f) ER_{pp}.

Geosci. Model Dev. Discuss., https://doi.org/10.5194/gmd-2018-286
Manuscript under review for journal Geosci. Model Dev.
Discussion started: 17 December 2018

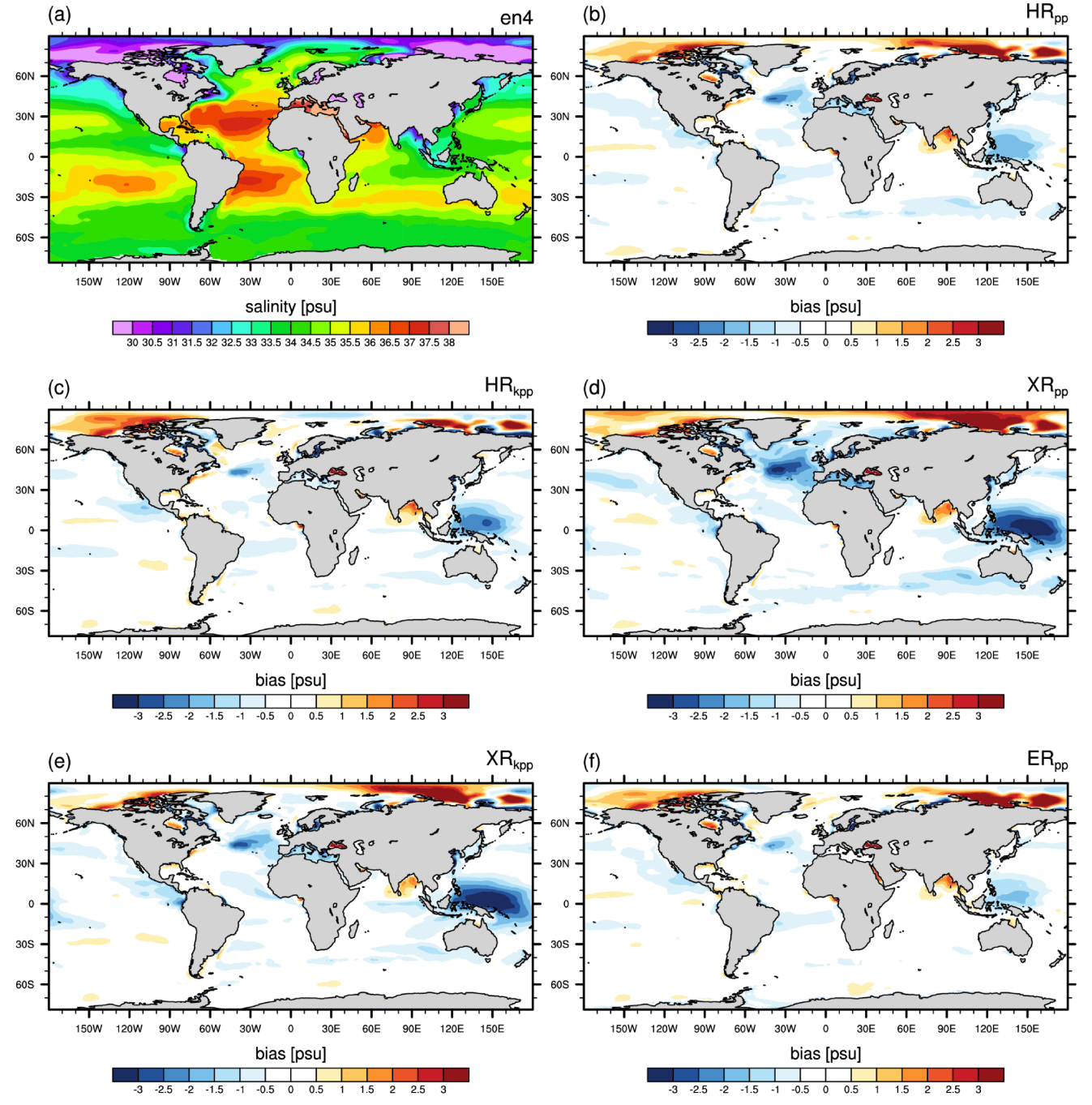

Figure 6. Sea surface salinity (psu) from (a) EN4 (averaged over 1945–1955) and for the differences: MPI-ESM1.2 minus EN4 for (b) HR_{pp},(c) HR_{kpp}, (d) XR_{pp}, and (e) XR_{kpp}, (f) ER_{pp}.

Geosci. Model Dev. Discuss., https://doi.org/10.5194/gmd-2018-286
Manuscript under review for journal Geosci. Model Dev.
Discussion started: 17 December 2018

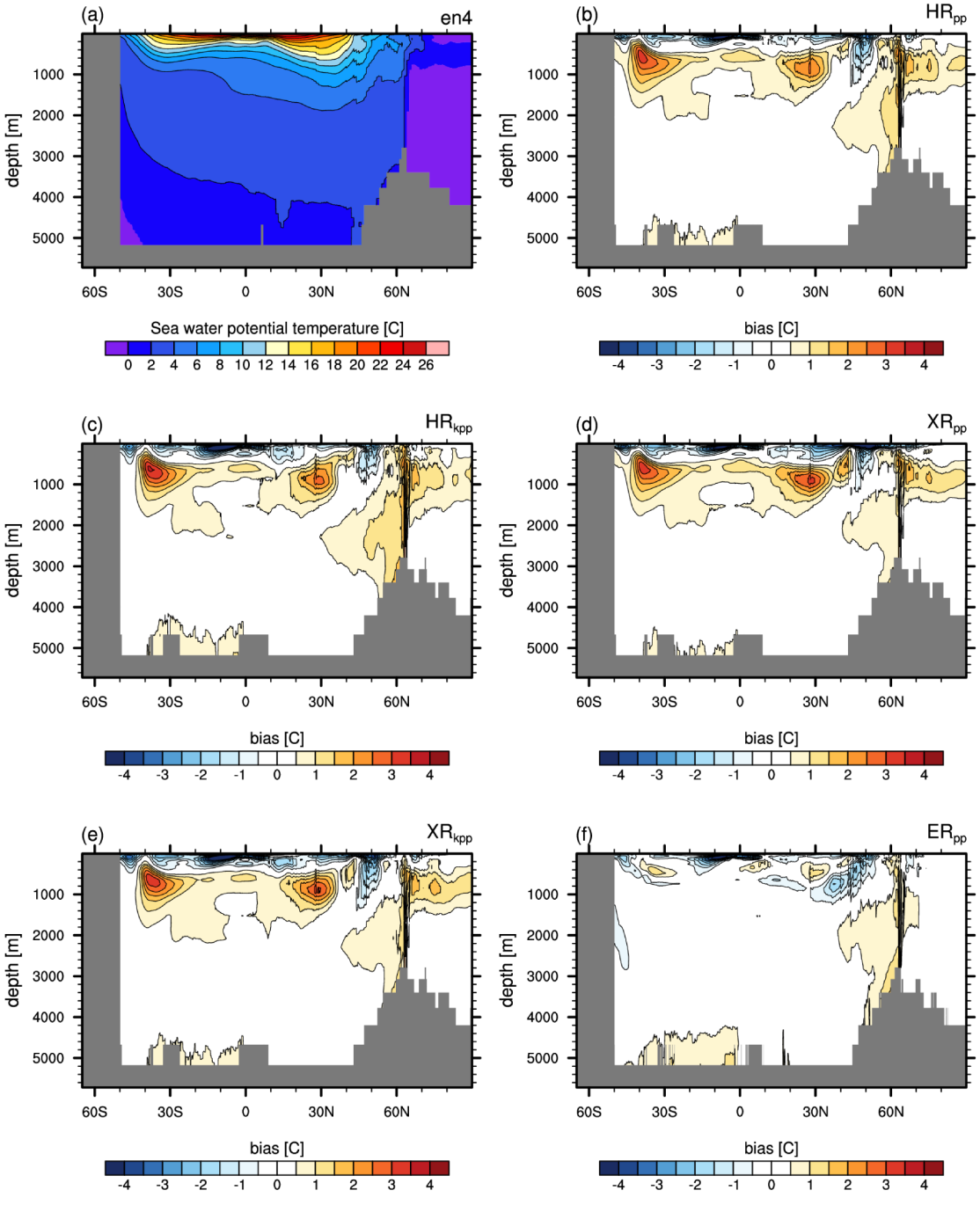

Figure 7. Zonal mean temperature transect through the Atlantic basin and the Arctic Ocean of (a) EN4 (averaged over 1945–1955) and the bias (MPI-ESM1.2 minus EN4) of (b) HR_{pp}, (c) HR_{kpp}, (d) XR_{pp}, (e) XR_{kpp}, and (f) ER_{pp}. Contour levels (b-f) begin with $\pm 0.5\,^{\circ}C$.

Geosci. Model Dev. Discuss., https://doi.org/10.5194/gmd-2018-286
Manuscript under review for journal Geosci. Model Dev.
Discussion started: 17 December 2018

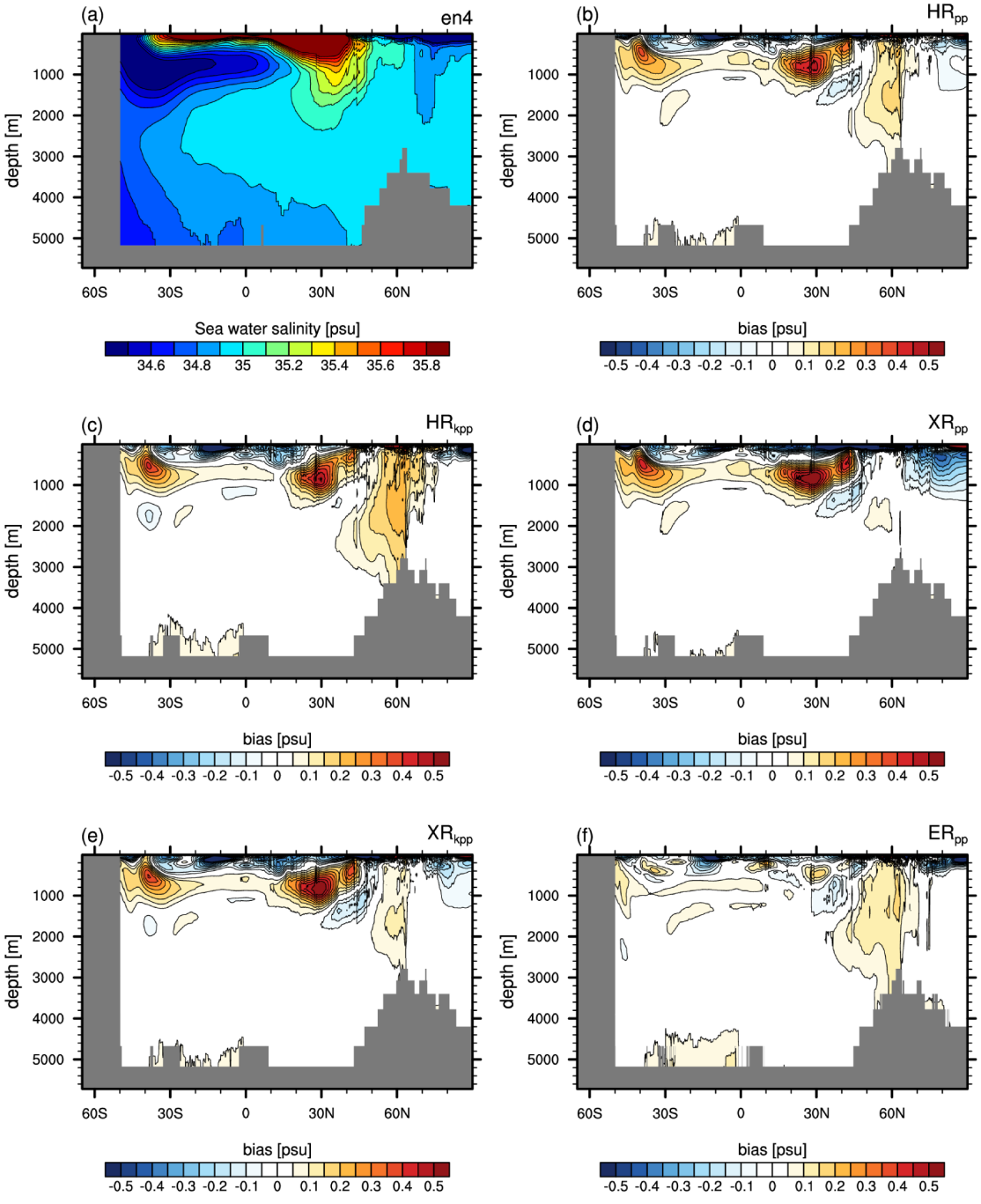

Figure 8. Zonal mean salinity transect through the Atlantic basin and the Arctic Ocean of (a) EN4 (averaged over 1945–1955) and the bias (MPI-ESM1.2 minus EN4) (b) HR_{kpp}, (c) XR_{pp}, and (d) XR_{kpp}. Contour levels (b-f) begin with ± 0.05 psu.

Geosci. Model Dev. Discuss., https://doi.org/10.5194/gmd-2018-286
Manuscript under review for journal Geosci. Model Dev.
Discussion started: 17 December 2018

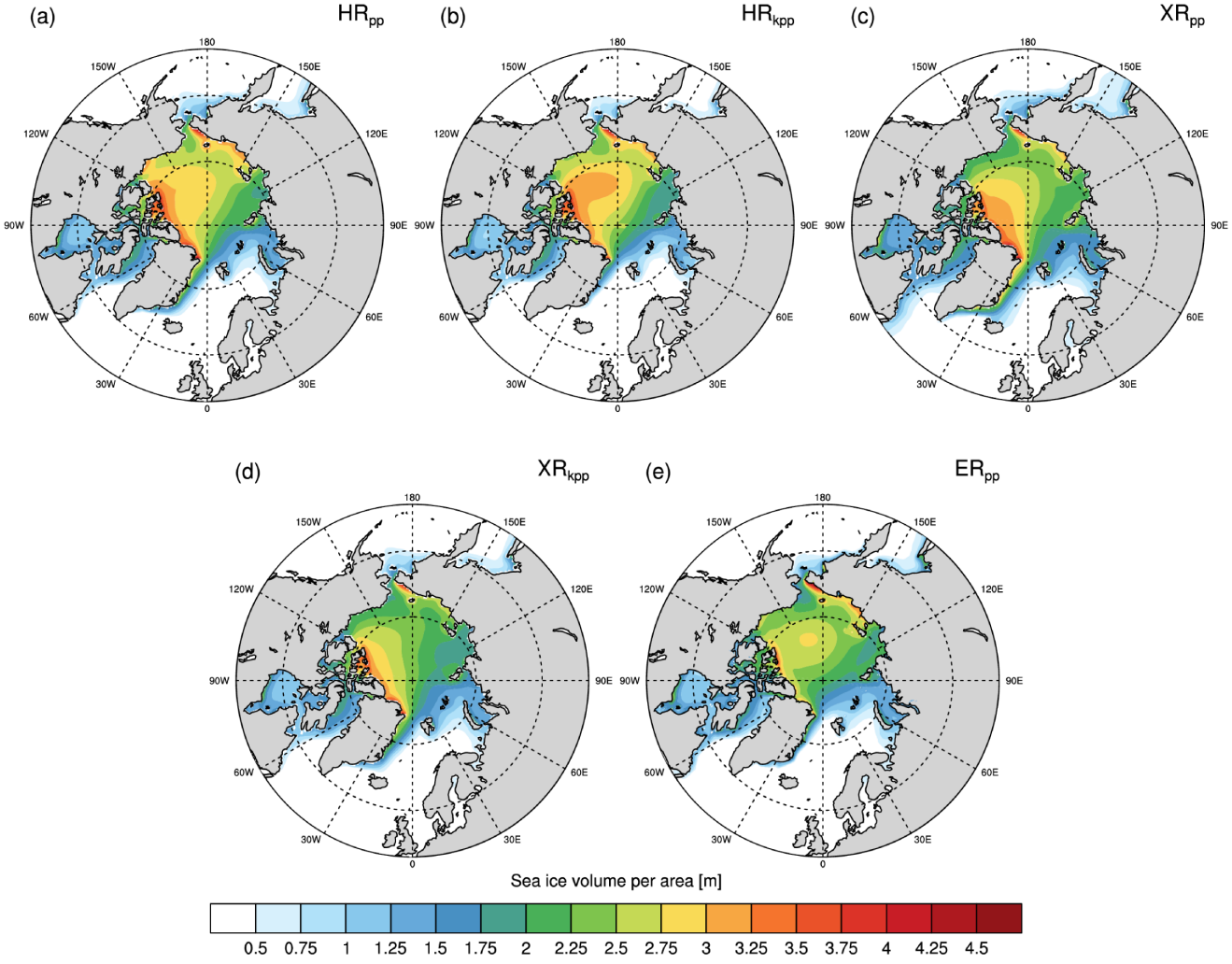

Figure 9. Time-averaged Arctic sea ice volume in March for (a) HR_{pp}, (b) HR_{kpp}, (c) XR_{pp}, (d) XR_{kpp}, and (e) ER_{pp}.

Geosci. Model Dev. Discuss., https://doi.org/10.5194/gmd-2018-286
Manuscript under review for journal Geosci. Model Dev.
Discussion started: 17 December 2018

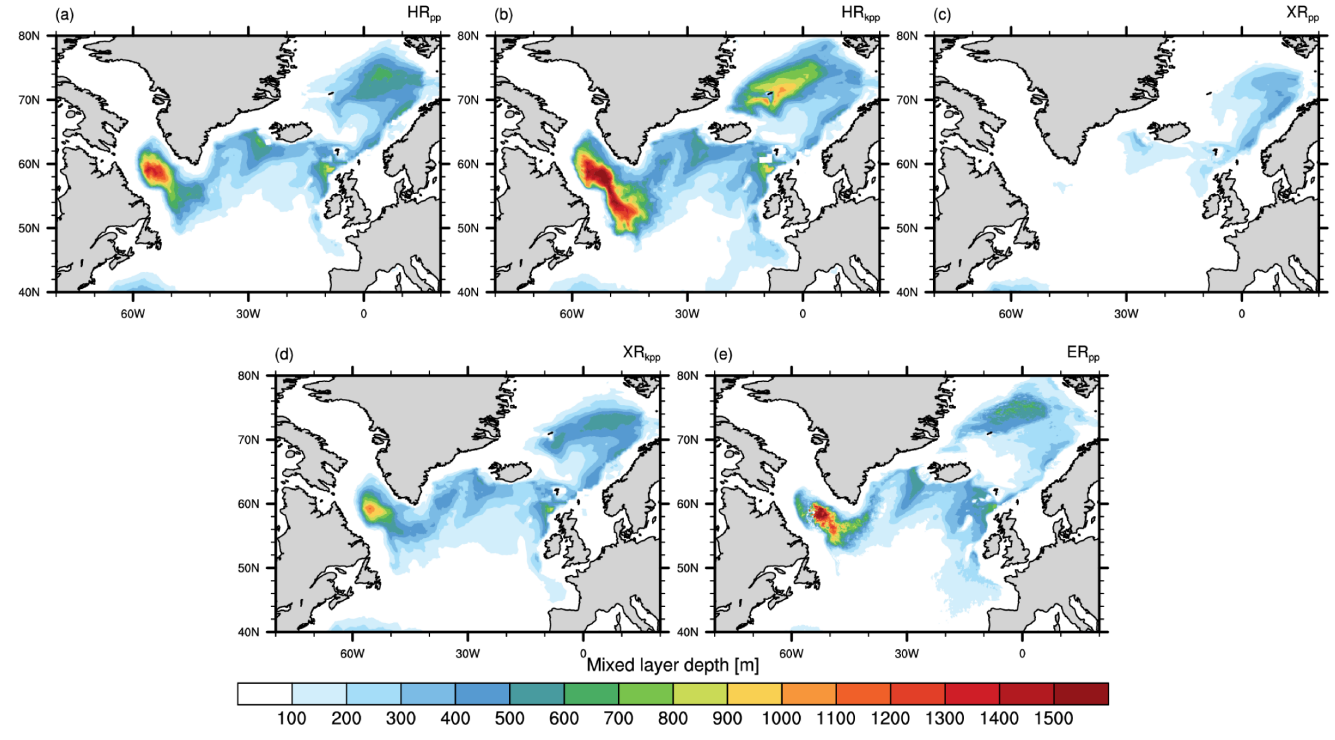

Figure 10. Time-averaged mixed layer depth ($\sigma_t = 0.01\,\mathrm{kg\,m^{-3}}$) in March in the North Atlantic and the Nordic Seas for (a) HR_{pp}, (b) HR_{kpp}, (c) XR_{pp}, (d) XR_{kpp}, and (e) ER_{pp}.

Geosci. Model Dev. Discuss., https://doi.org/10.5194/gmd-2018-286
Manuscript under review for journal Geosci. Model Dev.
Discussion started: 17 December 2018

Geoscientific Model Development Discussions
Open Access
EGU

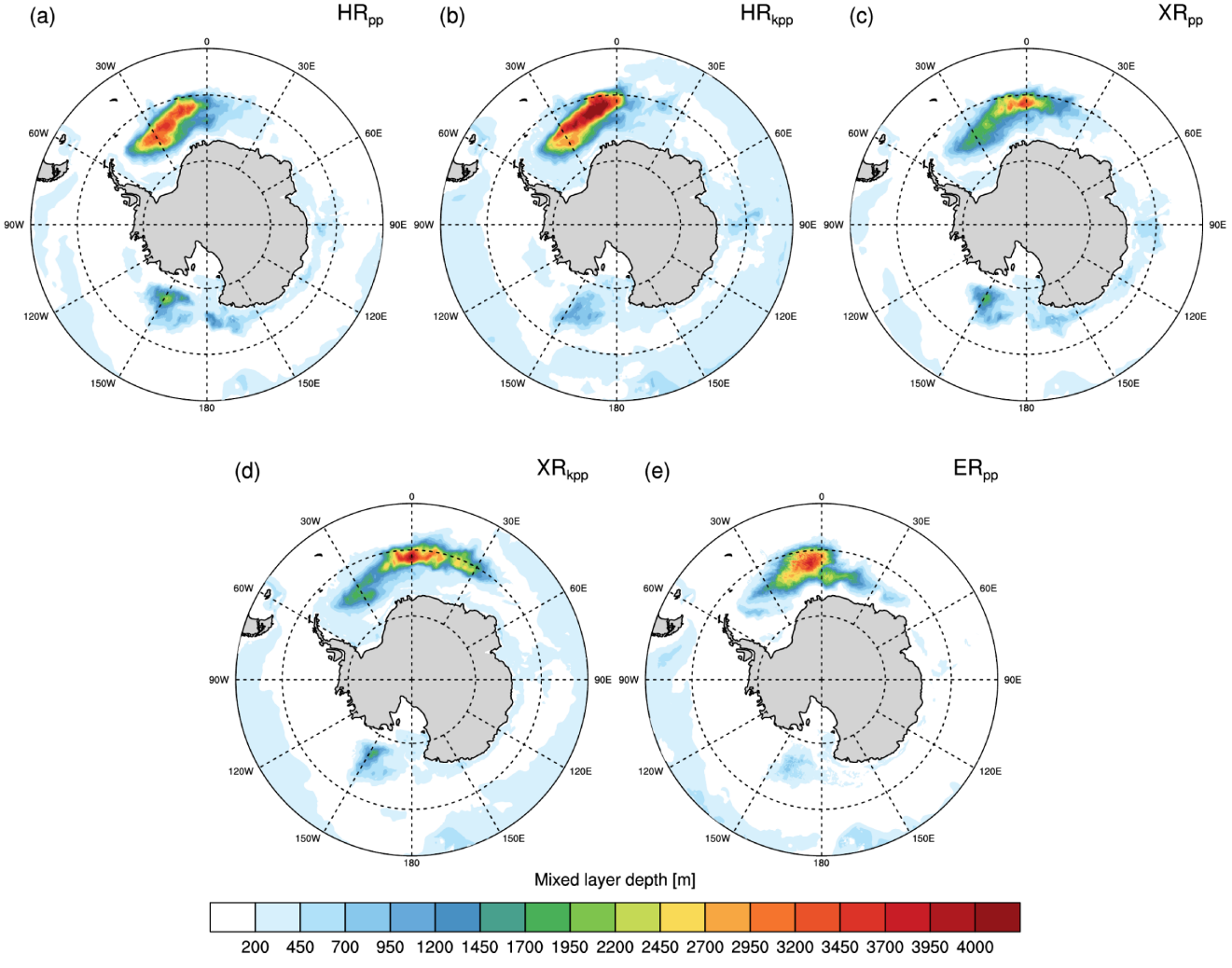

Figure 11. Time-averaged mixed layer depth ($\sigma_t = 0.03\,\mathrm{kg\,m^{-3}}$) in September in the Southern Ocean for (a) HR_{pp}, (b) HR_{kpp}, (c) XR_{pp}, (d) XR_{kpp}, and (e) ER_{pp}.

Geosci. Model Dev. Discuss., https://doi.org/10.5194/gmd-2018-286
Manuscript under review for journal Geosci. Model Dev.
Discussion started: 17 December 2018

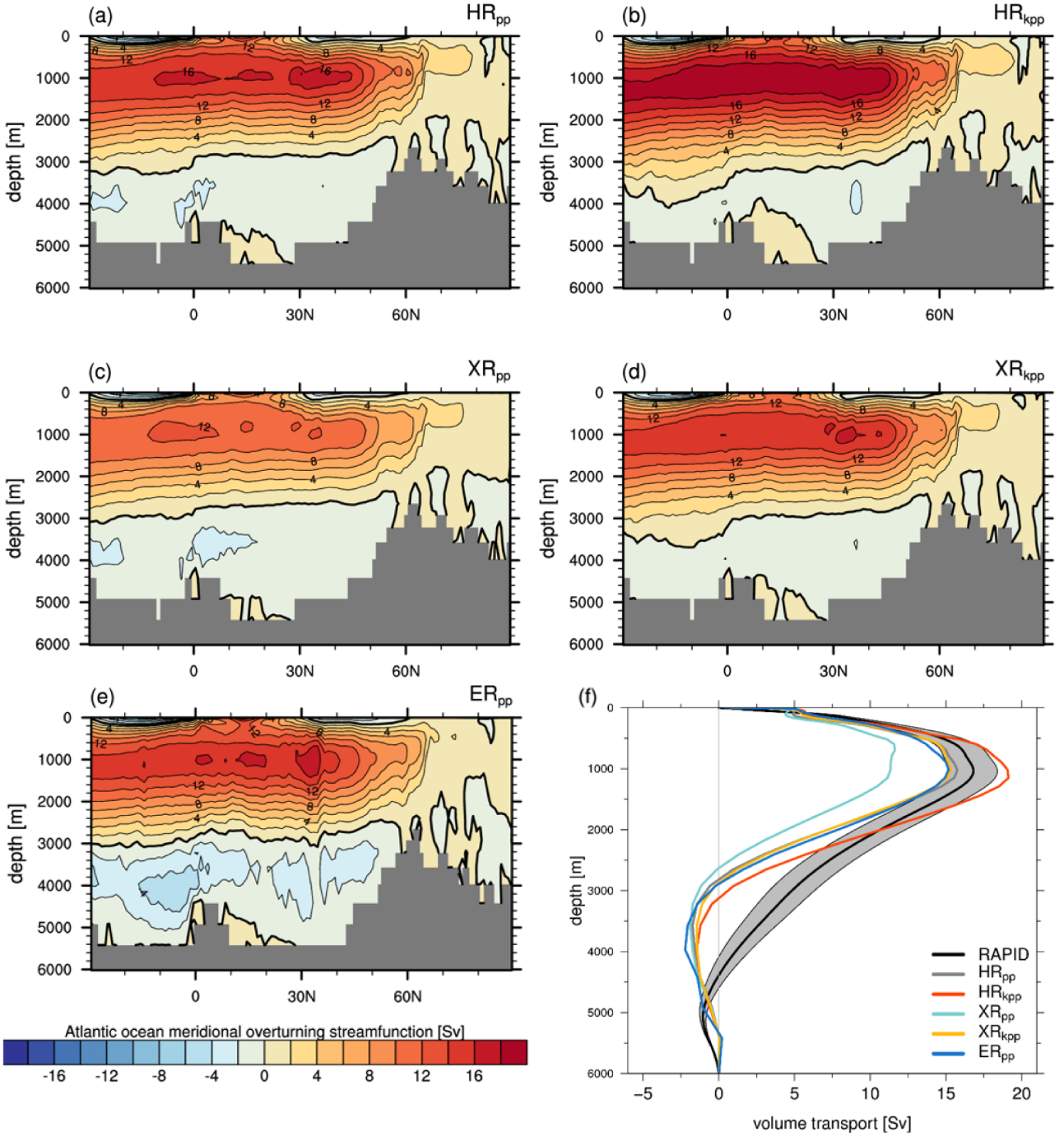

Figure 12. Eulerian stream function (Sv $:= 10^6\,\mathrm{m}^3\,\mathrm{s}^{-1}$) of the Atlantic Meridional Overturning Circulation (AMOC) for (a) HR_{pp},(b) HR_{kpp}, (c) XR_{pp}, (d) XR_{kpp}, and (e) ER_{pp}. The zero contour is drawn as a thicker line. In (f) annual mean profiles of the AMOC at 26.5 ° N are shown as observed from Apr 2004 to Feb 2017 by the RAPID-MOCHA-WBTS array (± one standard deviation marked by grey shading) (Smeed et al., 2017) and simulated by MPI-ESM1.2.

Geosci. Model Dev. Discuss., https://doi.org/10.5194/gmd-2018-286
Manuscript under review for journal Geosci. Model Dev.
Discussion started: 17 December 2018

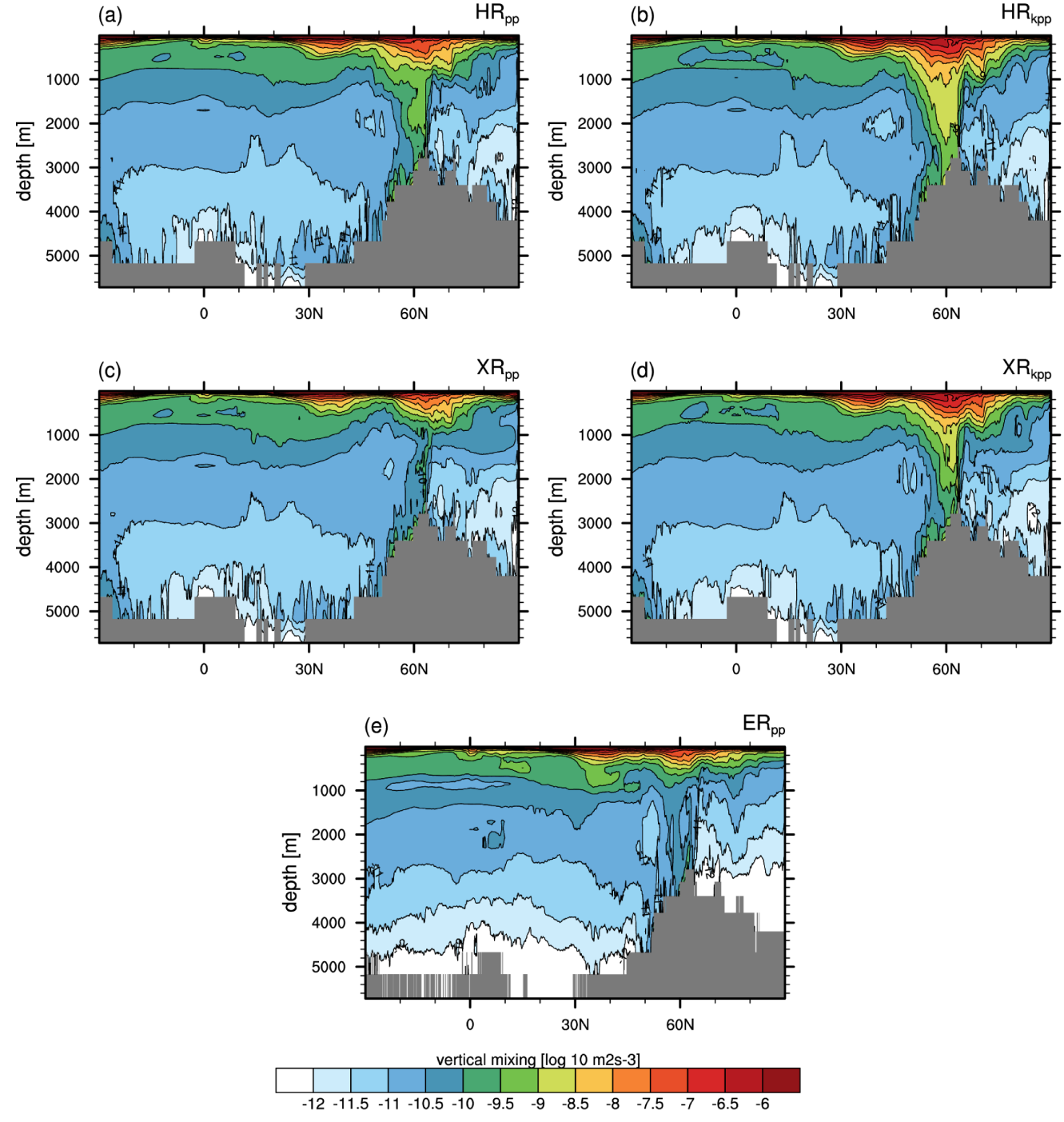

Figure A1. Transect of zonal mean vertical mixing ($log_{10}(k_v N^2)$) through the Atlantic basin and the Arctic Ocean of (a) HR_{pp}, (b) HR_{kpp}, (c) XR_{pp}, (d) XR_{kpp}, and (e) ER_{pp}.

Geosci. Model Dev. Discuss., https://doi.org/10.5194/gmd-2018-286
Manuscript under review for journal Geosci. Model Dev.
Discussion started: 17 December 2018

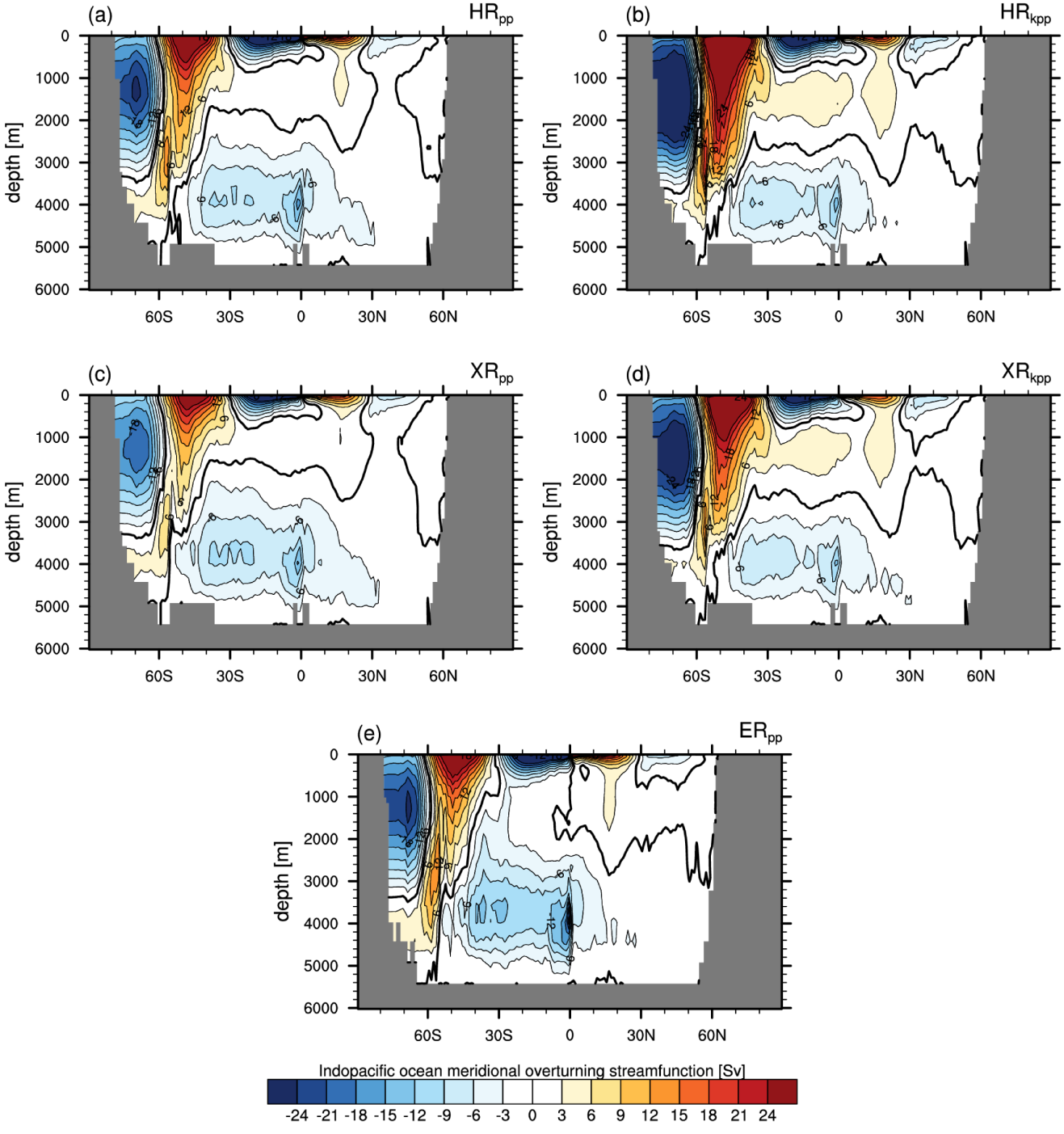

Figure A2. Eulerian stream function (Sv $:= 10^6\,\mathrm{m}^3\,\mathrm{s}^{-1}$) of the Pacific meridional overturning circulation for (a) $\mathrm{HR}_{\mathrm{pp}}$, (b) $\mathrm{HR}_{\mathrm{kpp}}$, (c) $\mathrm{XR}_{\mathrm{pp}}$, (d) $\mathrm{XR}_{\mathrm{kpp}}$, and (e) $\mathrm{ER}_{\mathrm{pp}}$. The zero contour is drawn as a thicker line.

Geosci. Model Dev. Discuss., https://doi.org/10.5194/gmd-2018-286
Manuscript under review for journal Geosci. Model Dev.
Discussion started: 17 December 2018

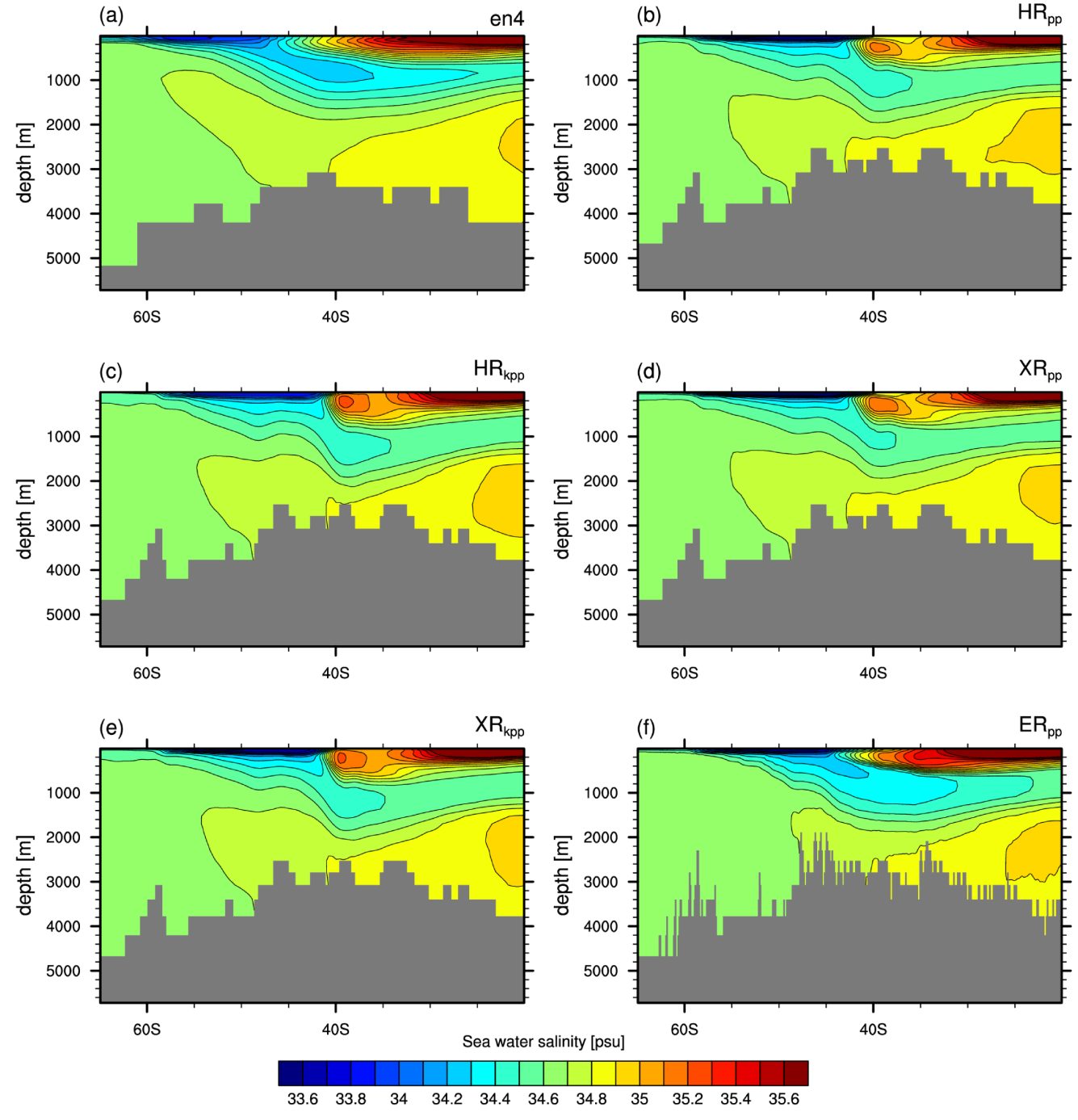

Figure A3. Time-mean salinity section along 15°W (from 65°S to 20°S) in the Southern Ocean of (a) EN4 (1945-1955), (b) HR_{pp}, (c) HR_{kpp}, (d) XR_{pp}, (e) XR_{kpp}, and (f) ER_{pp}.